Multiple critical points in effective quark models

Lorenzo Ferroni,[1,2] Volker Koch,[2] and Marcus B. Pinto[2,3]
[1]*Institut für Theoretische Physik, Goethe-Universität, Max-von-Laue St. 1, D-60438 Frankfurt am Main, Germany*
[2]*Nuclear Science Division, Lawrence Berkeley National Laboratory, 94720 Berkeley, California, USA*
[3]*Departamento de Fisica, Universidade Federal de Santa Catarina, 88040-900 Florianópolis, Santa Catarina, Brazil*
(Received 30 July 2010; revised manuscript received 11 October 2010; published 29 November 2010)

We consider the two-flavor version of the linear sigma model as well as of the Nambu–Jona-Lasinio model, at finite temperature and quark chemical potential, beyond the mean field approximation. Using parameter values for the pion and quark current masses which weakly break chiral symmetry, we show that both models can present more than one critical end point. In particular, we explicitly show that the appearance of a new critical point associated with a first-order line at high temperature and low densities could help to conciliate some lattice results with model predictions. Using different techniques, we perform an extensive thermodynamical analysis to understand the physical nature of the different critical points. For both models, our results suggest that the new first-order line which starts at vanishing chemical potential has a more chiral character than the usual line which displays a character more reminiscent of a liquid-gas phase transition.

DOI: 10.1103/PhysRevC.82.055205 PACS number(s): 11.10.Wx, 12.38.Aw, 12.39.Fe, 12.39.Ki

I. INTRODUCTION

Numerical analyses of quantum chromodynamics (QCD) on a discrete space-time lattice (lattice QCD) indicate that the transition from confined to deconfined matter at finite temperature T and vanishing quark chemical potential μ is a crossover [1]. On the other hand, model studies [2–5] predict a first-order transition to occur for μ of the order of 1/3 of the baryon mass and $T = 0$. In between these two regimes, a second-order critical point is expected in the T-μ plane at some intermediate values of T and μ. The existence and the exact location of the critical point is still a matter of dispute [6] and has been under intense theoretical study using effective field theory models of QCD [2,3,5,7–13] (see also the recent analysis performed in Ref. [14]). Unfortunately, a direct application of lattice QCD at finite μ is, at present, still quite problematic. Only relatively recently, new theoretical developments and technical improvements allowed one to circumvent in various ways the fermion determinant problem and start performing Monte Carlo calculations (see Ref. [15] for a review). Although most of the results obtained up to now seem to support the QCD critical point, an interesting observation against its existence comes from Ref. [16] where, from numerical simulations of QCD at imaginary chemical potential, one observes that the region of quark masses where the transition is presumably of the first order (for quark masses smaller than the physical ones) tends to shrink for small positive values of the chemical potential μ. Conversely, according to models supporting the critical point, the first-order region should expand when μ increases, so that the physical quark mass point hits the critical line at some finite values of T and μ. A possible explanation for this discordance has been given in Ref. [11], where it was pointed out that a strong (repulsive) vector coupling may account for the initial shrinkage of the first-order region, which would then start expanding again at larger values of μ. As a result, two critical points might appear for a given range of (small) quark masses, as argued in Ref. [13]. However, it has been remarked [11] that this does not necessarily imply the existence of the QCD critical point, since a too strong repulsive potential may in fact provoke the disappearance of the first-order line (and thus of the critical point) for physical quark masses. If the vector coupling is too small, instead, the initial shrinkage of the first-order region is not clearly seen. A recent estimate [17] of the vector coupling from flavor susceptibilities evaluated with lattice QCD seems to support the latter scenario.

Based on the analysis of the linear sigma model (LσM) with two-flavor quarks, it was shown in Refs. [12,13] that the inclusion of thermal fluctuations of the mesonic fields leads to the appearance of two critical points for a small finite vacuum pion mass, $m_\pi^0 < 50$ MeV, without the need for a vector interaction. For physical values of the pion mass, the model predicts only one critical point, as one would naively expect for QCD. Also in this case, the initial shrinkage of the first-order region at small μ was proved to be a not uncommon feature. However, as we will discuss, the direct transposition of these arguments to QCD should be done with special care. In the chiral limit and $\mu = 0$, in fact, the two-flavor LσM has a first-order transition, whereas in QCD, universality arguments [18] suggest also the possibility of a transition of the second order [of the O(4) universality class] depending on the strength of the $U_A(1)$ anomaly. Very recently, it was found (see Ref. [19]) that the correct treatment of the fermion vacuum fluctuations (which were neglected in most LσM applications) can change the order of the transition in the chiral limit from first to second order, depending on the coupling constants. In this case the phase diagram of the LσM would resemble the Nambu–Jona-Lasinio model (NJL) one with a second-order line starting at $\mu = 0$ and high T and terminating at a tricritical point (at intermediate T and μ) where the first-order line starts ending at $T = 0$.

Interestingly enough, these findings of Ref. [12] suggest the possibility of a rich structure for the QCD phase diagram in a situation which is similar to the one which arises in metamagnetic systems whose phase diagram may display two critical points in the magnetic field versus temperature

plane [20]. A multi-critical-point structure induced by charge neutrality and vector interaction has been recently discussed by Zhang and Kunihiro in the context of the $2+1$ flavor NJL model [14]. It is worth pointing out that the presence of strong magnetic fields ($B \simeq 10^{19}$ G) may change the order of the phase transition, as shown by Fraga and Mizher [21] who considered the two-flavor LσM, at $\mu = 0$, obtaining that the usual crossover can turn into a first-order phase transition in this regime.

The aim of the present work is to explore in some detail the phase diagram of two of the most important effective field theory models of QCD with two quark flavors represented by the LσM and the NJL model when small finite pion (and quark current) masses are considered. The thermodynamics of both models have been compared, with standard parametrization in Ref. [8] where the mean field approximation (MFA) has been used. As we shall see, going beyond the MFA allows the appearance of more than one critical point in both models for certain parameter values. For the LσM we will use the same approximation as in Ref. [12] and will closely follow the methods therein to map the phase diagram for various values of the pion mass, m_π^0. As it will be shown, by varying m_π^0, two and three critical points (two of them are actually very close to each other) may appear. As a further step, we will explore the nature of these critical points by analyzing the susceptibilities and correlations of the net-quark number density, the entropy density, and the scalar density.

The second part of the paper will be dedicated to the NJL model, in its simplest form, which will be treated in the so-called optimized perturbation theory (OPT). The OPT method (which also goes by different names or has many variants, e.g., delta expansion [22] and order-dependent mapping [23]) is well known for allowing evaluations beyond MFA due to the way it modifies ordinary perturbative expansion, giving a nontrivial (nonperturbative) coupling dependence. Examples of successful applications include the most precise analytical values of the critical temperature for noninteracting Bose gases [24,25] as well as the precise location of the tricritical point and the mixed liquid-gas phase within the Gross-Neveu model in $2+1$ dimensions [26]. The latter illustrates how this method can be a powerful tool beyond standard perturbation theory, since these important effects were missed by the MFA and could not be precisely determined by Monte Carlo simulations [27]. The OPT version adopted here is mainly indicated to nongauge theories, which (at finite temperature) require the method to be extended, e.g., by adding and subtracting a hard thermal loop improvement that modifies the propagators and vertices in a self-consistent way, in the so-called hard-thermal-loop perturbation theory (HTLpt) [28]. Regarding its use within renormalizable theories, the OPT has just been substantially improved by its combination with renormalization group properties [29].

This method has been recently applied to the NJL model in the evaluation of the thermodynamical potential beyond MFA, using standard parametrization [30]. The same type of application will be considered here, with a different set of parameters, in order to verify the possibility of multiple critical points as found in the LσM. Our investigation, as already anticipated, shows that in the very strong coupling limit this situation (which would be missed by the MFA) arises. It is interesting to remark that the OPT brings $1/N_c$ corrections to the MFA effective potential which are proportional to the scalar density, $\rho_s = \langle \bar{\psi}\psi \rangle$, as well as to the net-quark number density, $\rho_q = \langle \psi^+ \psi \rangle$, whose contribution to the pressure goes as $-G/(2N_f N_c)(2\rho_q^2 - \rho_s^2)$ where G is the usual NJL coupling, N_c is the number of colors, and N_f the number of flavors. This means that a type of $1/N_c$ suppressed vector term whose strength is twice its scalar counterpart will contribute to the pressure, so that when the interaction is sufficiently strong the results seem to support the findings of Ref. [11] where the SU(3) NJL with an explicit repulsive vector interaction, such as the one suggested in Ref. [31], was used. We recall that, contrary to the LσM, the NJL is a nonrenormalizable theory which is often regularized by a noncovariant ultraviolet cutoff[1] Λ. Then, from the quantitative point of view, our whole NJL application must be taken with care, since to generate exotic phase diagrams similar to the LσM one, we need very high values for G which in turn generate high effective quark masses at zero temperature and density. Although the effective quark mass value generated by those parameters becomes larger than Λ, the values of relevant observables, such as the quark condensate and the pion decay constant, remain well within reasonable values. Also, as already emphasized, one of the goals of the present NJL application is to check whether this model, like the LσM, supports the existence of more than one critical point in its phase diagram. After obtaining the OPT effective potential (or free energy density), we derive the pressure and many thermodynamical quantities of interest including susceptibilities and critical exponents. The results obtained with both models indicate that the first-order line observed at low chemical potential and high temperature has a more "chiral" character, while its low temperature and high chemical potential counterpart displays characteristics typical of a "liquid-gas" phase transition. Finally, it will be shown that with both models, our results seem to support the back-bending of the critical line in the μ-m_c plane (where m_c is the quark current mass) which, as first discussed in Refs. [11,13], could reconcile the actual lattice findings with most model predictions. It is also shown that the MFA completely misses the possibility of more than one critical point in the T-μ plane, for both models.

The paper is organized as follows. In the next section, the LσM is reviewed with the inclusion of thermal fluctuations. After obtaining the phase diagram in the T-μ plane for small pion masses, the characteristics of each different critical point is examined by a careful analysis of the densities and susceptibilities. In Sec. III, the recent OPT application [30] to the NJL model is quickly reviewed. Here, we show that a strong coupling and small current mass may lead to the emergence of a second critical point, analogous to the one found in the LσM. We perform a comprehensive thermodynamical analysis to investigate how multiple critical points appear in the T-μ plane as well as in phase coexistence diagrams in the T-ρ_B and P-$1/\rho_B$ planes. We also numerically investigate the behavior

[1] See Ref. [8] for an interesting discussion regarding how this difference may affect thermodynamical results.

of quantities such as the interaction measure, the equation of state parameter, bulk viscosity, and susceptibilities at, and around, each critical end point. The latter quantities allow us to estimate some relevant critical exponents in order to distinguish the physical nature of both critical points, which is also done by considering the free energy in terms of two ordering densities, ρ_s and ρ_q. Finally, in Sec. IV we present our main conclusions.

II. THE LINEAR SIGMA MODEL WITH QUARKS

In standard notation, the density Lagrangian of the LσM with quarks reads

$$\mathcal{L} = \tfrac{1}{2}(\partial_\mu \boldsymbol{\pi})^2 + \tfrac{1}{2}(\partial_\mu \sigma)^2 - U(\sigma, \boldsymbol{\pi}) + \bar{\psi}[i\gamma^\mu \partial_\mu - g(\sigma + i\gamma_5 \boldsymbol{\tau} \cdot \boldsymbol{\pi})]\psi, \tag{2.1}$$

where ψ is the flavor isodoublet spinor representing the quarks (u and d), and

$$U(\sigma, \boldsymbol{\pi}) = \frac{\lambda}{4}(\sigma^2 + \boldsymbol{\pi}^2 - f^2)^2 - H\sigma \tag{2.2}$$

is the classical potential energy density. In the chiral limit (obtained by setting $H = 0$ in the previous equation), the chiral symmetry $\mathrm{SU}(2)_V \times \mathrm{SU}(2)_A$ is spontaneously broken at the classical level, and the pion is the associated massless Goldston boson. For $H \neq 0$, the chiral symmetry is explicitly broken by the term $H\sigma$ in Eq. (2.2), which gives the pion a finite mass at $T = 0$ and $\mu = 0$. The scalar field σ has a finite vacuum expectation value v determined by the classical equation of motion

$$\lambda(v^2 - f^2)v - H = 0. \tag{2.3}$$

Accordingly, the σ field is conveniently expressed as a sum of the condensate plus fluctuations, $\sigma = v + \Delta$. In the LσM Lagrangian given by Eq. (2.1) there is no explicit mass term for the quark field, the quark mass being given only by the condensate, gv. The parameters of the model are given by the set of equations

$$H = f_\pi m_\pi^{0\,2}, \qquad \lambda = \frac{m_\sigma^{0\,2} - m_\pi^{0\,2}}{2f_\pi^2}, \qquad f^2 = \frac{m_\sigma^{0\,2} - 3m_\pi^{0\,2}}{m_\sigma^{0\,2} - m_\pi^{0\,2}} f_\pi^2, \qquad g = \frac{m_q^0}{f_\pi}, \tag{2.4}$$

where $f_\pi = 92.4$ MeV is the pion decay constant. Consistent with Refs. [12,32], we set the vacuum σ mass to $m_\sigma^0 = 700$ MeV and the quark mass to $m_q^0 = 313$ MeV (i.e., one-third of the nucleon mass). The last parameter that one needs to fix is the vacuum pion mass, m_π^0, which will be varied from 10 to 140 MeV.

A. Linearized mesonic action for the linear sigma model with quarks

To calculate the equation of state of the model, we closely follow the self-consistent method first proposed in Ref. [32] and used also in Ref. [12]. Accordingly, we write the grand canonical partition function as a functional integral in Euclidean space with the imaginary time $\tau = it$

$$Z = \mathrm{Tr}\exp[-\beta(\widehat{H} - \mu\widehat{N})] = \int \mathcal{D}\psi\mathcal{D}\bar{\psi}\mathcal{D}\sigma\mathcal{D}\boldsymbol{\pi}\exp\left\{\int_0^\beta d\tau \int_V d^3x(\mathcal{L} + \mu\bar{\psi}\gamma_0\psi)\right\}, \tag{2.5}$$

where $\widehat{H}$ and $\widehat{N}$ are the Hamiltonian and the net-quark number operator, respectively. In Eq. (2.5), $\beta = 1/T$ is the inverse temperature, μ is the quark chemical potential,[2] and V is the system volume. Following the same steps as in Refs. [12,32], we now integrate away the quark degrees of freedom. This amounts to calculating the partition function of the quark sector

$$Z_{q\bar{q}} = \int \mathcal{D}\psi\mathcal{D}\bar{\psi}\exp\left\{\int_0^\beta d\tau \int_V d^3x\,\bar{\psi}\widehat{D}\psi\right\}, \tag{2.6}$$

where

$$\widehat{D} = -\gamma^0\partial_\tau + i\boldsymbol{\gamma}\cdot\nabla - g(\sigma + i\gamma_5\boldsymbol{\tau}\cdot\boldsymbol{\pi}) + \mu\gamma^0. \tag{2.7}$$

The Gaussian integral in Eq. (2.6) can be solved with standard techniques [33] and yields

$$Z_{q\bar{q}} = \det\widehat{D}. \tag{2.8}$$

In Ref. [34] an expression such as Eq. (2.8) has been expanded in a series of commutators involving the derivatives of the mesonic fields. In our analysis we will discard these terms, implicitly assuming that the meson mode amplitudes vary slowly in space and time (the same approximation was introduced also in Refs. [12,32]). The determinant in Eq. (2.8) can then be evaluated as for the free case. After performing a Fourier transformation in momentum-frequency space and using the property

$$\ln\det\widehat{D} = \mathrm{Tr}\ln\widehat{D}, \tag{2.9}$$

we finally obtain

$$\ln\det\widehat{D} = \frac{N_c N_f}{\beta V}\sum_{\boldsymbol{p},n}\ln\left\{\beta^2\left[\omega_n^2 + (\varepsilon - \mu)^2\right]\right\} + \ln\left\{\beta^2\left[\omega_n^2 + (\varepsilon + \mu)^2\right]\right\}, \tag{2.10}$$

where $N_f = 2$, $N_c = 3$, and ω_n are the Matsubara frequencies taking the values $\omega_n = (2n+1)\pi T$ because of the antiperiodicity condition on the fermionic functional integral $\psi(\boldsymbol{x}, 0) = -\psi(\boldsymbol{x}, \beta)$. In Eq. (2.10), $\varepsilon = \sqrt{p^2 + m_q^2}$ is the energy, with the quark effective mass

$$m_q^2 = g^2(\boldsymbol{\pi}^2 + \sigma^2). \tag{2.11}$$

We note that Eq. (2.10) is formally identical to the standard result except for the dependence of m_q on the mesonic fields. Performing the summation over the Matsubara frequencies in Eq. (2.10), one then obtains

$$\ln Z_{q\bar{q}}(\sigma, \boldsymbol{\pi}) = -\int_0^\beta d\tau \int_V d^3x\,\Omega_{q\bar{q}}(\sigma, \boldsymbol{\pi}),$$
$$\Omega_{q\bar{q}}(\sigma, \boldsymbol{\pi}) = -\frac{N_c N_f T}{\pi^2}\int dp\; p^2\{\beta\varepsilon + \ln[1 + e^{-\beta(\varepsilon-\mu)}] + \ln[1 + e^{-\beta(\varepsilon+\mu)}]\}. \tag{2.12}$$

[2] In this work, we use the quark chemical potential μ. The baryochemical potential is $\mu_B = 3\mu$.

Since we are interested in the low-energy properties of the model, we will ignore (as was done in Refs. [12,13]), for simplicity, the shift in the zero point energy. The effect of such a contribution at finite temperature has been analyzed in Ref. [32] for $m_\pi = 138$ MeV. For physical values of the pion mass, this is not expected to change the qualitative behavior of the model. As we pointed out in the Introduction, however, the effect of the fermion vacuum loop could actually play an important role, changing the order of the transition in the chiral limit at $\mu = 0$ from first to second order [19]. These contributions are taken into account in the NJL model, where they are responsible of the dynamical breaking of the chiral symmetry.

Using the result in Eq. (2.12) we can now write an effective Lagrangian that includes only the mesonic degrees of freedom

$$\mathcal{L} = \tfrac{1}{2}(\partial_\mu \boldsymbol{\pi})^2 + \tfrac{1}{2}(\partial_\mu \sigma)^2 - U_{\text{eff}}(\sigma, \boldsymbol{\pi}), \tag{2.13}$$

where

$$U_{\text{eff}}(\sigma, \boldsymbol{\pi}) = U(\sigma, \boldsymbol{\pi}) - \frac{T}{V} \ln Z_{q\bar{q}}(\sigma, \boldsymbol{\pi}). \tag{2.14}$$

The Euler-Lagrange equations then read

$$\begin{aligned} \partial_\mu \partial^\mu \sigma + \frac{\partial U_{\text{eff}}(\sigma, \boldsymbol{\pi})}{\partial \sigma} &= 0, \\ \partial_\mu \partial^\mu \pi_i + \frac{\partial U_{\text{eff}}(\sigma, \boldsymbol{\pi})}{\partial \pi_i} &= 0, \qquad i = 1, 2, 3. \end{aligned} \tag{2.15}$$

We now proceed to linearize the mesonic action by taking the average $\langle \cdots \rangle$ of the equations of motion over the field fluctuations. First we decompose, as before, the σ field as $\sigma = v + \Delta$ where $v = \langle \sigma \rangle$ and Δ is the fluctuation. Of course, $\langle \Delta^n \rangle = 0$ when n is odd, and the same is true for $\langle \boldsymbol{\pi}^n \rangle$. Therefore, since the pion fluctuations always occur as $\boldsymbol{\pi}^2$, the average $\langle \partial U_{\text{eff}}/\partial \pi_i \rangle = 0$, whereas from the first one of the Eqs. (2.15) we get the condition for the condensate

$$\left\langle \frac{\partial U_{\text{eff}}(v + \Delta, \boldsymbol{\pi})}{\partial \Delta} \right\rangle = \left\langle \frac{\partial U_{\text{eff}}(v + \Delta, \boldsymbol{\pi})}{\partial v} \right\rangle = 0. \tag{2.16}$$

The meson masses are then identified with the average of the second derivative of the effective potential

$$m_\sigma^2 = \left\langle \frac{\partial^2 U_{\text{eff}}(v + \Delta, \boldsymbol{\pi})}{\partial \Delta^2} \right\rangle, \quad m_\pi^2 = \left\langle \frac{\partial^2 U_{\text{eff}}(v + \Delta, \boldsymbol{\pi})}{\partial \pi_i^2} \right\rangle, \tag{2.17}$$

and the effective potential is linearized as

$$\begin{aligned} U_{\text{eff}}(v + \Delta, \boldsymbol{\pi}) \sim \langle U_{\text{eff}}(v + \Delta, \boldsymbol{\pi}) \rangle &+ \tfrac{1}{2} m_\sigma^2 (\Delta^2 - \langle \Delta^2 \rangle) \\ &+ \tfrac{1}{2} m_\pi^2 (\boldsymbol{\pi}^2 - \langle \boldsymbol{\pi}^2 \rangle). \end{aligned} \tag{2.18}$$

The two terms $1/2 m_\sigma^2 \Delta^2$ and $1/2 m_\pi^2 \boldsymbol{\pi}^2$ on the right-hand side of the last equation are the mass terms to be added to the kinetic energy in the mesonic Lagrangian to give the mesonic partition function

$$\begin{aligned} Z_{\sigma;\boldsymbol{\pi}} &= \int \mathcal{D}\sigma \mathcal{D}\boldsymbol{\pi} \exp\left\{ \frac{1}{2} \int_0^\beta d\tau \int_V d^3x \left[(\partial_\mu \boldsymbol{\pi})^2 + (\partial_\mu \sigma)^2 \right.\right. \\ &\quad \left.\left. - m_\sigma^2 \Delta^2 - m_\pi^2 \boldsymbol{\pi}^2 \right] \right\} \\ &= \exp\left[-\frac{V}{T} (\Omega_\sigma + \Omega_\pi) \right], \end{aligned} \tag{2.19}$$

where[3]

$$\begin{aligned} \Omega_\sigma &= \frac{T}{2\pi^2} \int dp\ p^2 \left[\frac{1}{2} \beta \varepsilon_\sigma + \ln\left(1 - e^{-\beta \varepsilon_\sigma}\right) \right], \\ \Omega_\pi &= \frac{3T}{2\pi^2} \int dp\ p^2 \left[\frac{1}{2} \beta \varepsilon_\pi + \ln\left(1 - e^{-\beta \varepsilon_\pi}\right) \right], \end{aligned} \tag{2.20}$$

and

$$\varepsilon_\sigma = \sqrt{p^2 + m_\sigma^2}, \qquad \varepsilon_\pi = \sqrt{p^2 + m_\pi^2}. \tag{2.21}$$

Stemming from Eq. (2.19), we have two self-consistency relations between the meson masses and the corresponding fluctuations

$$\langle \Delta^2 \rangle = 2 \frac{\partial \Omega_\sigma}{\partial m_\sigma^2}, \qquad \langle \boldsymbol{\pi}^2 \rangle = 2 \frac{\partial \Omega_\pi}{\partial m_\pi^2}. \tag{2.22}$$

Finally, we write the thermodynamic potential density as[4]

$$\begin{aligned} \Omega &= -\frac{T}{V} \ln Z \\ &= \langle U_{\text{eff}} \rangle - \frac{1}{2} m_\sigma^2 \langle \Delta^2 \rangle - \frac{1}{2} m_\pi^2 \langle \boldsymbol{\pi}^2 \rangle + \Omega_\sigma + \Omega_\pi. \end{aligned} \tag{2.23}$$

The average over the field fluctuations is performed by using the techniques of Refs. [32,35,36]. Given an arbitrary functional $\mathcal{O}(v + \Delta, \boldsymbol{\pi}^2)$ we can write the Taylor expansion around $\Delta = \boldsymbol{\pi}^2 = 0$ and take the average term by term

$$\langle \mathcal{O}(v + \Delta, \boldsymbol{\pi}^2) \rangle = \sum_{n,k=0}^{\infty} \frac{\partial^{n+k} \mathcal{O}(v + \Delta, \boldsymbol{\pi}^2)}{\partial \Delta^n \partial \boldsymbol{\pi}^{2k}} \bigg|_{\Delta = \boldsymbol{\pi}^2 = 0} \left\langle \frac{\Delta^n \boldsymbol{\pi}^{2k}}{n!k!} \right\rangle. \tag{2.24}$$

By using the relation derived in Ref. [35], we then relate the terms $\langle \Delta^n \boldsymbol{\pi}^{2k} \rangle$ to powers of $\langle \Delta^2 \rangle$ and $\langle \boldsymbol{\pi}^2 \rangle$, i.e., $\langle \Delta^n \rangle = (n-1)!! \langle \Delta^2 \rangle^{n/2}$ and $\langle \boldsymbol{\pi}^{2k} \rangle = (2k+1)!! \langle \boldsymbol{\pi}^2/3 \rangle^k$, which amounts to summing up the infinite series of daisy and superdaisy diagrams in the Hartree approximation. The resulting expression turns out to be equivalent to an integration over a Gaussian distribution [32]

$$\langle \mathcal{O}(v + \Delta, \boldsymbol{\pi}^2) \rangle = \int_0^\infty dz P_\sigma(z) \int dy y^2 P_\pi(y) \mathcal{O}(v + z, y^2), \tag{2.25}$$

where

$$\begin{aligned} P_\sigma(z) &= \frac{1}{\sqrt{2\pi \langle \Delta^2 \rangle}} \exp\left(-\frac{z^2}{2\langle \Delta^2 \rangle} \right), \\ P_\pi(y) &= \sqrt{\frac{2}{\pi}} \left(\frac{3}{\langle \boldsymbol{\pi}^2 \rangle} \right)^{3/2} \exp\left(-\frac{3y^2}{2\langle \boldsymbol{\pi}^2 \rangle} \right). \end{aligned} \tag{2.26}$$

In the following, we will need to perform derivatives of the average value of some quantities such as the thermodynamic potential density Ω. After two integration by parts, using

[3] Also for these terms we ignore the shift in the zero point energy, as was done in Ref. [12].

[4] In the following, where not needed, we will avoid writing explicitly the dependence of the functionals on σ and $\boldsymbol{\pi}^2$.

Eqs. (2.25) and (2.26), one can obtain the following useful relation [32]:

$$\frac{\partial}{\partial\alpha}\langle\mathcal{O}(v+\Delta,\boldsymbol{\pi}^2)\rangle = \frac{\partial v}{\partial\alpha}\left\langle\frac{\partial\mathcal{O}(v+\Delta,\boldsymbol{\pi}^2)}{\partial v}\right\rangle + \frac{1}{2}\frac{\partial\langle\Delta^2\rangle}{\partial\alpha}\left\langle\frac{\partial^2\mathcal{O}(v+\Delta,\boldsymbol{\pi}^2)}{\partial\Delta^2}\right\rangle + \frac{1}{2}\frac{\partial\langle\boldsymbol{\pi}^2\rangle}{\partial\alpha}\left\langle\frac{\partial^2\mathcal{O}(v+\Delta,\boldsymbol{\pi}^2)}{\partial\pi_i^2}\right\rangle. \quad (2.27)$$

With Eq. (2.27), and Eqs. (2.16) and (2.17), it is not difficult to see that

$$\frac{\partial\Omega}{\partial v} = \left\langle\frac{\partial U_{\rm eff}}{\partial v}\right\rangle + \frac{1}{2}\frac{\partial\langle\Delta^2\rangle}{\partial v}\left(\left\langle\frac{\partial^2 U_{\rm eff}}{\partial\Delta^2}\right\rangle - m_\sigma^2\right) + \frac{1}{2}\frac{\partial\langle\boldsymbol{\pi}^2\rangle}{\partial v}\left(\left\langle\frac{\partial^2 U_{\rm eff}}{\partial\pi_i^2}\right\rangle - m_\pi^2\right) = 0. \quad (2.28)$$

In a similar way, using the Eqs. (2.22) one can also easily show that

$$\frac{\partial\Omega}{\partial m_\sigma^2} = \frac{\partial\Omega}{\partial m_\pi^2} = 0. \quad (2.29)$$

Equations (2.28) and (2.29) guarantee the consistency of the approach and the standard connection between thermodynamic and statistical mechanics [37]. The equation of state of the system is given by the simultaneous solutions in the variables v, m_σ, m_π of Eqs. (2.16) and (2.17), with the field fluctuations given by Eq. (2.29). In Ref. [12] this was done numerically, and the authors found a rich phase structure with one or two critical points, depending on the value of vacuum pion mass m_π^0. In the next section, we will repeat the same calculation as in Ref. [12], and we will show that another critical point (very difficult to detect) appears in the phase diagram.

B. The phase diagram

We now proceed and map the phase diagram of the model for various values of the vacuum pion mass ranging from $m_\pi = 10$ MeV to $m_\pi = 140$ MeV. As a first step, we need to find a way to localize the first-order line(s) and the critical end point(s). This is usually done by looking at the change in shape of the thermodynamic potential across a transition line.

This method (which will be adopted for the NJL model in Sec. III) allows us to see quite clearly the onset (and usually the order) of a phase transition, but unfortunately it cannot be used for the present analysis. Our approximation is, in fact, based on an expansion of the thermodynamic potential around a minimum, and our equations are defined only there, so a different method must be employed. A typical signature of the onset of a first-order transition is the presence of two minima of the thermodynamic potential, corresponding to the high- and low-temperature phases. In turn, we should see two distinct solutions for v, m_σ, m_π at the same T and μ. The transition happens when these two solutions have the same potential (pressure), i.e., the point when the system switches from one minimum to the other. For each value of μ, we solve the system of equations starting from low temperatures (the broken phase[5]) and following the line of minima increasing the temperature by a small amount ΔT at each step, using the latest solution as the initial point for the solving routine. Once we are sure to be in the high-T symmetric phase, we solve the system of equations backward (going from high to small T) until we are sure to be below the transition temperature. If the transition is continuous, we will find a unique solution for each value of T. Conversely, if the transition is of the first order, we will have a region where two solutions exist at the same T.

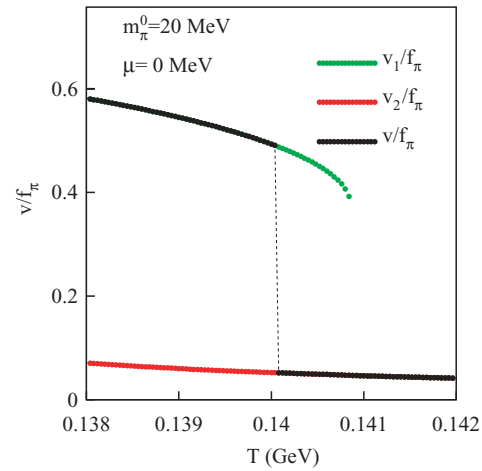

FIG. 1. (Color online) Condensate v (normalized to f_π) as a function of the temperature in the vicinity of the first-order transition for $m_\pi^0 = 20$ MeV and $\mu = 0$. The stable solution v (shown with black markers and the dashed line) is the one that corresponds to the highest pressure. The other two (metastable) solutions v_1 and v_2 are also shown.

In Fig. 1, this is shown for the condensate v around the transition line for $m_\pi^0 = 20$ MeV. For this value of the pion mass, the system undergoes a first-order transition at $T \sim 140$ MeV and $\mu = 0$. As one can see, the solution corresponding to the symmetry-broken phase (v_1) exists at low T and shortly above the transition temperature, whereas the symmetric solution (v_2) exists at high T and below the transition. The actual solution (the one corresponding to the greater pressure) is shown by black dots and the dashed line.

With this method, we now map the phase diagram of the model in the T-μ plane. Our results are consistent with those in Ref. [12], where the authors performed the same calculation and found that for sufficiently small values of the vacuum pion mass ($m_\pi^0 \lesssim 50$ MeV), the system has two critical points. In Fig. 2, we plot the phase diagram of the model in the MFA [Fig. 2(a)] and with the inclusion of mesonic fluctuations [Fig. 2(b)]. In Fig. 2(b), we have analyzed various values of $m_\pi^0 = 10, 20, 35, 50, 140$ MeV. For $m_\pi^0 = 10$ MeV, the phase diagram is divided into two parts by a continuous first-order line. For $m_\pi^0 = 20$ and 35 MeV, the first-order line is interrupted by a continuous region; and for some

[5]Since the symmetry is explicitly broken by the vacuum pion mass, expressions such as "symmetric phase" or "broken phase" must be understood just as a nomenclature convention.

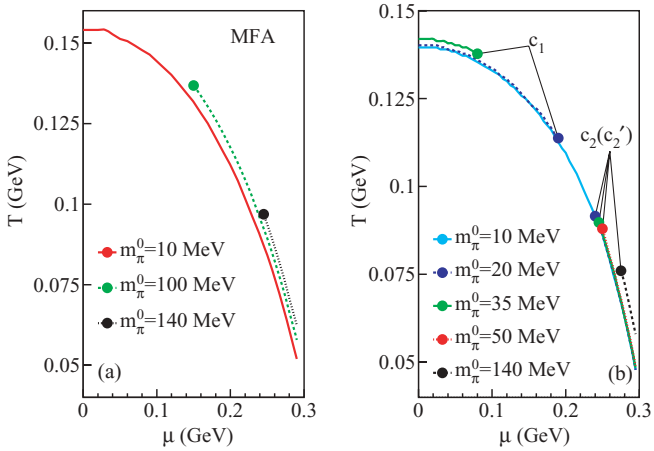

FIG. 2. (Color online) Left panel: the phase diagram of the LσM in the MFA for $m_\pi^0 = 10$, 100, and 140 MeV. Right panel: the phase diagram of the LσM with the inclusion of mesonic fluctuations for $m_\pi^0 = 10$, 20, 35, 50, 140 MeV.

$35 < m_\pi^0 \leqslant 50$ MeV, the branch at low μ disappears and we have the usual continuous transition at low μ and first order at high μ.

The leftmost branch of the first-order line (when it exists) ends in a critical point. For the rightmost one, the situation seems to be different. A closer look reveals the presence of a double critical point. This is shown in Fig. 3(a) for $m_\pi^0 =$ 35 MeV. As one can see, the first-order line bifurcates and ends in *two* critical points, which have been labeled c_2 and c_2'. Their existence is revealed by the presence of two first-order transitions that have been detected, as before, looking at the double solutions of our system of equations. In Fig. 3(b), we show the parameter v along the dashed line crossing the two first-order lines in Fig. 3(a). As one can see, there are two distinct solutions (which we have checked to correspond to minima of the thermodynamic potential) for two slightly different (∼1 MeV) values of the temperature, indicating a double first order.

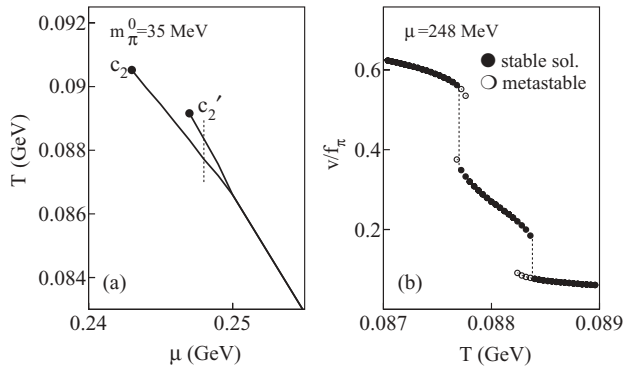

FIG. 3. (a) Detail of the phase diagram for $m_\pi^0 = 35$ MeV showing the rightmost first-order line bifurcating and ending in two critical points. (b) Condensate v (normalized to f_π) as a function of the temperature for $\mu = 248$ MeV. The plotted region corresponds to the dashed vertical line crossing the two first-order lines in (a). The stable solution is represented by black dots and the metastable solutions by open circles.

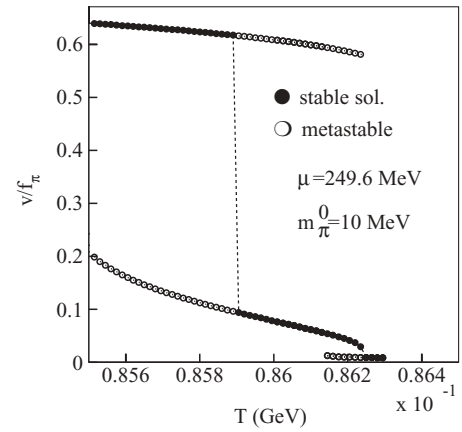

FIG. 4. Condensate v (normalized to f_π) as a function of temperature for $\mu = 249.6$ MeV and $m_\pi^0 = 10$ MeV. Two first-order transitions are visible at $T \sim 85.9$ and $T \sim 86.2$ MeV. The stable solution is represented by black dots and the metastable solutions by open circles.

A similar behavior can be observed for all the explored values of the pion mass, i.e., 20, 35, 50, and 140 MeV. Also for $m_\pi = 10$ MeV, where the transition is of the first order everywhere, a very short branch of the the first-order line appears around $\mu \sim 250$ MeV and $T \sim 86$ MeV, producing another very short branch ending in a critical point at $\mu \sim 249$ MeV and $T \sim 87$ MeV. The situation is qualitatively similar to the one in Fig. 3(a) except for the fact that the leftmost critical point c_2 does not exist as the first-order line continues until $\mu = 0$. In Fig. 4, one can see the multiple solutions for v, indicating the two first-order lines at $T \sim 85.9$ and $T \sim 86.2$ MeV, respectively. For the rightmost transition, the discontinuity in v is very small, but its presence is proved by the existence of the metastable solution. At present the reason for the this unusual bifurcation of the high-μ first-order line is not understood and requires further study. It may simply be an artifact of the approximation (mean field plus fluctuations) used for the treatment of the linear sigma model. However, as we will see in the next section, despite their vicinity in the phase diagram, the two first-order lines appear to have slightly different qualitative features.

C. Densities and susceptibilities

We now go one step further and analyze the susceptibilities in the LσM with the aim of characterizing the critical point(s) by studying the fluctuations of the net-quark number density ρ_q, scalar density ρ_s, and entropy density s in the vicinity of the critical regions. By definition, the quark density is

$$\rho_q = \frac{T}{V}\frac{\partial \ln Z}{\partial \mu} = -\frac{\partial \Omega}{\partial \mu}. \tag{2.30}$$

By using Eqs. (2.27)–(2.29), one then has

$$\rho_q = -\left\langle \frac{\partial U_{\text{eff}}}{\partial \mu} \right\rangle = \frac{T}{V}\left\langle \frac{\partial \ln Z_{q\bar{q}}}{\partial \mu} \right\rangle. \tag{2.31}$$

To calculate the scalar density, it is convenient to introduce a mass term $-\eta\bar{\psi}\psi$ for the quarks in the Lagrangian in Eq. (2.1), where η is a fictitious bare quark mass to be set to zero

afterward. This amounts to a thermal quark mass

$$m_q^2 = g^2\boldsymbol{\pi}^2 + (g\sigma + \eta)^2. \tag{2.32}$$

From the partition function written as in Eq. (2.5), one then sees that

$$\rho_s = \langle\bar{\psi}\psi\rangle = -\frac{T}{V}\frac{\partial \ln Z}{\partial \eta}\bigg|_{\eta=0} = \frac{\partial\Omega}{\partial\eta}\bigg|_{\eta=0}, \tag{2.33}$$

that is, as before,

$$\rho_s = \left\langle\frac{\partial U_{\rm eff}}{\partial\eta}\right\rangle_{\eta=0} = -\frac{T}{V}\left\langle\frac{\partial \ln Z_{q\bar{q}}}{\partial\eta}\right\rangle_{\eta=0}. \tag{2.34}$$

Unlike the quark density in Eq. (2.31), the scalar density can be directly evaluated, once v and the meson masses are known, without the need to solve any further integral. Indeed, from Eq. (2.16), one gets

$$\frac{T}{V}\left\langle\frac{\partial \ln Z_{q\bar{q}}}{\partial v}\right\rangle = \lambda(v^2 + 3\langle\Delta^2\rangle + \langle\boldsymbol{\pi}^2\rangle - f^2)v - H. \tag{2.35}$$

Noting that

$$\frac{\partial \ln Z_{q\bar{q}}}{\partial\eta} = \frac{\partial \ln Z_{q\bar{q}}}{\partial v}\frac{\partial m^2}{\partial\eta}\left(\frac{\partial m^2}{\partial v}\right)^{-1} = \frac{1}{g}\frac{\partial \ln Z_{q\bar{q}}}{\partial v}, \tag{2.36}$$

and using Eqs. (2.34) and (2.35), we finally obtain

$$\rho_s = \frac{1}{g}[H - \lambda(v^2 + 3\langle\Delta^2\rangle + \langle\boldsymbol{\pi}^2\rangle - f^2)v]. \tag{2.37}$$

The net-quark number density and the scalar density are the thermodynamic variables conjugate to μ and the fictitious quark mass η, respectively. The last density that we need to evaluate is the the entropy density (conjugate to the temperature T), i.e.,

$$s = -\frac{\partial\Omega}{\partial T} = \left\langle\frac{1}{V}\ln Z_{q\bar{q}} + \frac{T}{V}\frac{\partial \ln Z_{q\bar{q}}}{\partial T}\right\rangle - \frac{\partial\Omega_\sigma}{\partial T} - \frac{\partial\Omega_\pi}{\partial T}. \tag{2.38}$$

In what follows, we will always assume the same number of u and d quarks in the system. The isospin density is therefore always vanishing for any value of T, μ, and η, and, of course, the same is true for its derivatives with respect to these quantities. The isospin density, therefore, does not mix with the other degrees of freedom[6] (ρ_q, ρ_s, and s) and will not be considered in our analysis at this time.

We can now go ahead and calculate the 3×3 covariance matrix as

$$\mathbf{C} = T\begin{pmatrix} \frac{\partial\rho_q}{\partial\mu} & -\frac{\partial\rho_q}{\partial\eta} & \frac{\partial\rho_q}{\partial T} \\ \frac{\partial\rho_s}{\partial\mu} & -\frac{\partial\rho_s}{\partial\eta} & \frac{\partial\rho_s}{\partial T} \\ \frac{\partial s}{\partial\mu} & -\frac{\partial s}{\partial\eta} & \frac{\partial s}{\partial T} \end{pmatrix} \equiv \mathbf{C}_{ij}, \quad i,j = 1,2,3. \tag{2.39}$$

This matrix is symmetric and can be diagonalized. We call e_1, e_2, e_3 the three eigenvalues of $\mathbf{C}$, and $\mathbf{u}, \mathbf{v}, \mathbf{z}$ the corresponding eigenvectors. Each one of the three eigenvectors can be related to a different orthogonal combination of the three original densities ρ_q, ρ_s, and s

$$\begin{aligned} \rho_{\mathbf{u}} &= u_1\rho_q + u_2\rho_s + u_3 s, \\ \rho_{\mathbf{v}} &= v_1\rho_q + v_2\rho_s + v_3 s, \\ \rho_{\mathbf{z}} &= z_1\rho_q + z_2\rho_s + z_3 s. \end{aligned} \tag{2.40}$$

These three new densities are now independent. At the critical point, only one of them will have divergent fluctuations, whereas the other two will remain finite. We chose, as a convention, to order the eigenvalues from the biggest e_1 to the smallest e_3. At the critical point, we then expect the first eigenvalue, e_1, to diverge. According to Eq. (2.40), the three components of the corresponding eigenvector $\mathbf{u} = (u_1, u_2, u_3)$ will then give us the expression of the critical density in terms of the original densities ρ_q, ρ_s, and s.

It is worth mentioning that in our analysis, the correlations between ρ_q and s are positive, whereas the correlations between ρ_s and s, and ρ_s and ρ_q are negative. This is because, at the transition, the thermal contribution to the scalar density drops from its maximum value (in the broken phase) to a very small value (exactly zero in the chiral limit) in the symmetric phase (see Ref. [32]), whereas both s and ρ_q exhibit the opposite behavior, going from smaller values (in the broken phase) to higher values (in the symmetric phase). Unlike s and ρ_q the scalar density is, in fact, dominated by the zero-point contributions. With their inclusion, one recovers the physically expected behavior [32]. One must then bear in mind that the following results are relevant for the thermal part of the model. Our general conclusions, however, are in agreement with the results obtained with the NJL in Sec. III where the zero-point contributions are included.

We analyze two different values for the vacuum pion mass: $m_\pi^0 = 35$ MeV (Figs. 5 and 6) and $m_\pi^0 = 140$ MeV (Fig. 7). We remind the reader here that we have chosen to label with c_1 the critical end point of the leftmost first-order line (if there is any) that starts at $\mu = 0$ and $T \sim 140$ MeV in the phase diagram. With c_2 and c_2' we refer to the two critical end points of the first-order line (which ultimately splits in two) that starts at $T = 0$ and $\mu \sim 300$ MeV, c_2' being the rightmost of the two as in Fig. 3. As we have seen in the last section, for $m_\pi^0 = 10$ MeV there is only the critical point c_2'. We will not consider that case here, however.

We begin with c_1 for $m_\pi^0 = 35$ MeV. In Figs. 5(a)–5(d), we show the three diagonal components of the covariance matrix ($\mathbf{C}_{11}, \mathbf{C}_{22}, \mathbf{C}_{33}$), and the three off-diagonal components ($\mathbf{C}_{12}$, $\mathbf{C}_{13}$, $\mathbf{C}_{23}$) for $\mu = 70$ and $\mu = 86$ MeV. For $\mu = 70$ MeV, the system undergoes a first-order phase transition at $T = 138.6$ MeV, whereas for $\mu = 86$ MeV the transition is continuous (but still very sharp) and takes place at $T = 137$ MeV. In between, one finds the unusual critical point c_1. By looking at the elements of the covariance matrix for these two values of μ, one sees that the dominant fluctuations are given by the entropy density and the scalar density. This is shown in Figs. 5(a) and 5(b), where the dominant diagonal terms in the vicinity of the transition are $\mathbf{C}_{22} = T\partial\rho_s/\partial\eta$ and $\mathbf{C}_{33} = T\partial s/\partial T$. From the off-diagonal terms in Figs. 5(c) and 5(d), one notices that the scalar and the entropy density are the most

[6]Note that even though the correlations with the other densities vanish, the isospin susceptibility (i.e. the derivative of the isospin with respect to the isospin chemical potential) does not.

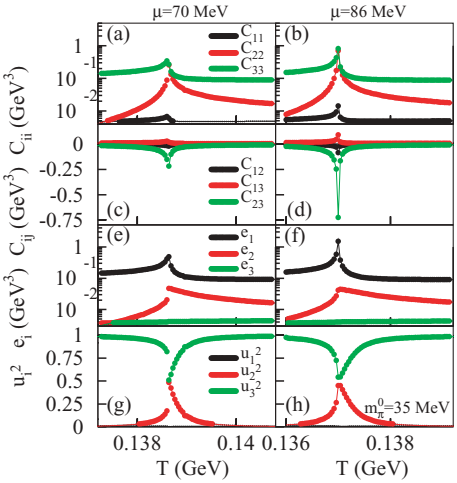

FIG. 5. (Color online) Panels (a) and (b): diagonal matrix elements of the covariance matrix as a function of temperature in the vicinity of the critical point c_1 for $m_\pi^0 = 35$ MeV and $\mu = 70$ and $\mu = 86$ MeV, respectively. Panels (c) and (d): off-diagonal matrix elements of the covariance matrix as a function of the temperature in the vicinity of the critical point c_1 for $m_\pi^0 = 35$ MeV and $\mu = 70$ and $\mu = 86$ MeV, respectively. Panels (e) and (f): eigenvalues of the covariance matrix as a function of temperature in the vicinity of the critical point c_1 for $m_\pi^0 = 35$ MeV and $\mu = 70$ and $\mu = 86$ MeV, respectively. Panels (g) and (h): square components of the (normalized) eigenvector corresponding to the larger eigenvalue (e_1) of the covariance matrix as a function of temperature in the vicinity of the critical point c_1 for $m_\pi^0 = 35$ MeV and $\mu = 70$ and $\mu = 86$ MeV, respectively.

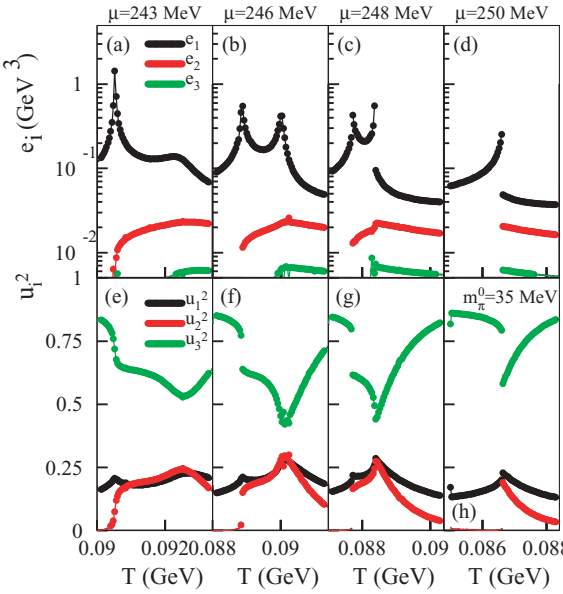

FIG. 6. (Color online) Panels (a)–(d): eigenvalues of the covariance matrix as a function of temperature in the vicinity of the critical points c_2 and c_2' for $m_\pi^0 = 35$ MeV and $\mu = 243$, 246, 248, and 250 MeV. Panels (e)–(h): square components of the (normalized) eigenvector corresponding to the larger eigenvalue (e_1) of the covariance matrix as a function of temperature in the vicinity of the critical point c_2 and c_2' for $m_\pi^0 = 35$ MeV and $\mu = 243$, 246, 248, and 250 MeV.

strongly anticorrelated (the magnitude of $\mathbf{C}_{23} = T\partial\rho_s/\partial T$ is much larger than the other off-diagonal coefficients). This fact can be observed in a more direct way by looking at the eigenvalue e_1 and the corresponding eigenvector $\mathbf{u}$. In Figs. 5(e) and 5(f), the three eigenvalues of the covariance matrix are plotted for the same range of values of T and μ. The largest eigenvalue e_1 is the only one showing a peak (it should actually diverge at the critical point). The eigenvector $\mathbf{u}$ [see Eq. (2.40)] gives us the three components of the critical density $\rho_\mathbf{u} = u_1\rho_q + u_2\rho_s + u_3 s$. As one can see, from Figs. 5(g) and 5(h), the critical density $\rho_\mathbf{u}$ is a mixture of almost solely the scalar and the entropy density (the first component u_1 does not appear in the plot, since it is always very close to zero).

As we have already discussed, in addition to this critical point the system exhibits two more critical points (c_2 and c_2') in the high-μ region (see Fig. 3). The analysis of these two points is shown in Fig. 6, where the three eigenvalues and the square components of the eigenvector $\mathbf{u}$ corresponding to e_1 are plotted for $\mu = 243$, 246, 248, and 250 MeV. For $\mu = 243$ MeV [Figs. 6(a) and 6(b)], the transition is continuous, but one can already clearly distinguish two peaks in the value of e_1 that are associated with the two critical points. The first one on the left (the one corresponding to c_2) is very sharp, while the other (a little bit on the right, corresponding to c_2') looks still like a bump. For $\mu = 246$ MeV [Figs. 6(b) and 6(f)], we have a first-order and a continuous transition. The first peak on the left is now a discontinuity, whereas the bump becomes sharper as the critical point c_2' is approached. For $\mu = 248$ MeV, we have a double first-order line [Fig. 6(c) and 6(g)]; and for $\mu = 250$ MeV, the two first-order lines have merged together to form a single transition line.

Looking at the square components of $\mathbf{u}$ in the lower panels of Fig. 6 one immediately sees that the density ρ_q is now playing a relevant role and its fluctuations are of the same order as those of the scalar density.

The two critical points c_2 and c_2', indeed, show different features. From the analysis of the diagonal matrix, one sees (lower panels in Fig. 6) that the critical density $\rho_\mathbf{u}$ is in both cases dominated by the entropy density. However, for point c_2 [see Figs. 6(a) and 6(e)], the scalar component is rather small [Fig. 6(e)] and overcomes the net-quark number density component only at a temperature immediately higher than the one corresponding to the peak of the eigenvalue e_1 [compare to Fig. 6(a)]. For the critical point c_2', instead, the critical density $\rho_\mathbf{u}$ is $\sim 50\%$ entropy density and the remnant 50% is almost equally split between net-quark and scalar density [see Fig. 6(f)].

The same analysis has been repeated for $m_\pi^0 = 140$ MeV in Fig. 7 in the vicinity of the two critical points c_2 and c_2' (the point c_1 does not exist) for $\mu = 275$, 277, 278, and 280 MeV. Once again, for $\mu = 275$ MeV the transition is continuous, whereas for $\mu = 277$ MeV we have a first-order and a continuous transition (corresponding to the rightmost spike), for $\mu = 278$ MeV we have a double first-order line, and finally for $\mu = 280$ MeV the two first-order lines have merged together to form a single one. By looking at the square

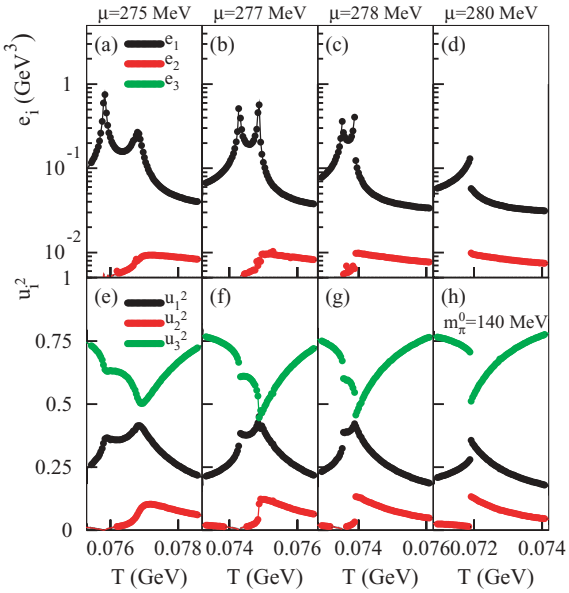

FIG. 7. (Color online) Panels (a)–(d): eigenvalues of the covariance matrix as a function of temperature in the vicinity of the critical points c_2 and c_2' for $m_\pi^0 = 140$ MeV and $\mu = 275$, 277, 278, and 280 MeV. Panels (e)–(h): square components of the (normalized) eigenvector corresponding to the larger eigenvalue (e_1) of the covariance matrix as a function of temperature in the vicinity of the critical point c_2 and c_2' for $m_\pi^0 = 140$ MeV and $\mu = 275$, 277, 278, and 280 MeV.

components of **u** (lower panels in Fig. 7), one can see that now the fluctuations of both critical points are dominated by the net-quark density and the entropy density. Even though in this case the scalar density plays only a minor role, it behaves in an even more visibly different way in the two critical points c_2 and c_2'. In Fig. 7 (panels a and e) at $T = 75.8$ MeV we are very close to the critical point c_2. In correspondence to this temperature, the scalar component of the critical density u_2^2 is suddenly suppressed [this can be seen, with some difficulty, in Fig. 7(e)]. At the same time, further inspections revealed that the correlations between ρ_s and ρ_q and the correlations between ρ_s and s cross zero. Indeed, in correspondence to the leftmost critical point c_2, the scalar density seems to behave as a "spectator" of the critical phenomenon, since it does not mix with the other densities. This is not the case for the critical point c_2'. Even though smaller than the entropy and net-quark number density components, the critical density now has a nonvanishing scalar contribution [Fig. 7(f)].

Increasing the mass of the pion, the critical points c_2 and c_2' move to the right of the phase diagram toward higher values of the chemical potential and lower temperature. As a result, the fluctuations of the net-quark number density become more important. In contrast, the critical point c_1 (when it exists) has only a minor component of the net-quark number density, and the transition is dominated by the entropy density and the scalar density, reflecting a more "chiral" behavior. This is in part due to the fact that the critical point c_1 exists only when the vacuum pion mass is small, i.e., when the chiral symmetry is only slightly (explicitly) broken.

III. THE NAMBU–JONA-LASINIO MODEL

Let us now consider the standard version of the two-flavor NJL model which is described by [38]

$$\mathcal{L} = \bar{\psi}[i\gamma_\mu \partial^\mu - m_c]\psi + G[(\bar{\psi}\psi)^2 + (\bar{\psi} i\gamma_5 \boldsymbol{\tau}\psi)^2], \tag{3.1}$$

where ψ (a sum over flavors and color degrees of freedom is implicit) represents a flavor isodoublet (u and d type of quarks) N_c-plet quark fields, while $\boldsymbol{\tau}$ are isospin Pauli matrices. The Lagrangian density (3.1) is invariant under (global) $\mathrm{U}(2)_f \times \mathrm{SU}(N_c)$ and, when $m_c = 0$, the theory is also invariant under chiral $\mathrm{SU}(2)_V \times \mathrm{SU}(2)_A \times \mathrm{U}(1)_V$ groups. Note that, as emphasized in Refs. [31,39], the introduction of a vector interaction term of the form $(\bar{\psi}\gamma^\nu\psi)^2$ in Eq. (3.1) is also allowed by the chiral symmetry, and such a term can become important at finite densities, generating a saturation mechanism depending on the vector coupling strength that provides better matter stability. Regarding analytic nonperturbative evaluations, one can consider one-loop contributions dressed up by a fermionic propagator, whose effective mass is determined in a self-consistent way. This approximation is known under different names, e.g., Hartree, large-N_c, or mean-field approximations. To obtain the effective potential (or Landau free energy density) for the quarks, U_{eff}, it is convenient to consider the bosonized version of the NJL, which is easily obtained by introducing auxiliary fields $(\sigma, \boldsymbol{\pi})$ through a Hubbard-Stratonovich transformation. Then, to introduce the auxiliary bosonic fields and to render our results more suitable to compare with the large-N_c approximation, it is convenient to use $G \to \lambda/(2N_c)$ and to formally treat N_c as a large number, which is set to the relevant value, $N_c = 3$, at the end of the evaluations. One then has

$$\mathcal{L} = \bar{\psi}(i\gamma_\mu \partial^\mu - m_c)\psi - \bar{\psi}(\sigma + i\gamma_5 \boldsymbol{\tau}\cdot\boldsymbol{\pi})\psi - \frac{N_c}{2\lambda}(\sigma^2 + \boldsymbol{\pi}^2). \tag{3.2}$$

The Euler-Lagrangian equations show that $\sigma = -(\lambda/N_c)\bar{\psi}\psi = -2G\bar{\psi}\psi$ and $\boldsymbol{\pi} = -(\lambda/N_c)\bar{\psi} i\gamma_5 \boldsymbol{\tau}\psi = -2G\bar{\psi} i\gamma_5 \boldsymbol{\tau}\psi$.

A. Optimized perturbation theory for the NJL model

The basic idea of the OPT method is to deform the original Lagrangian density by adding a quadratic term such as $(1-\delta)\eta\bar{\psi}\psi$ to the original Lagrangian density as well as multiplying all coupling constants by δ. The new parameter δ is just a bookkeeping label, and η represents an *arbitrary* mass parameter.[7] Perturbative calculations are then performed in powers of the dummy parameter δ which is formally treated as small and set to the original value, $\delta = 1$, at the end.[8] Therefore, the fermionic propagators are dressed by η which may also be viewed as an infrared regulator in the case of

[7] Note that although we have kept the same notation, the η used here has a completely different role than the one used previously in the LσM.

[8] Recall that within the large-N_c one performs an expansion in powers of $1/N_c$ where N_c is formally treated as large but set to the original value ($N_c = 3$ in our case) at the end.

massless theories. After a physical quantity, such as $U_{\rm eff}$, is evaluated to the order k and δ is set to unity, a residual η dependence remains. Then, optimal nonperturbative results can be obtained by requiring that $U_{\rm eff}^{(k)}(\eta)$ be evaluated where it is less sensitive to variations of the arbitrary mass parameter. This requirement translates into the criterion known as the principle of minimal sensitivity (PMS) [40]

$$\left.\frac{dU_{\rm eff}{}^{(k)}(\eta)}{d\eta}\right|_{\bar\eta,\delta=1}=0. \tag{3.3}$$

In general, the solution to this equation implies self-consistent relations generating a nonperturbative G dependence. In most cases, nonperturbative $1/N_c$ corrections appear already at the first nontrivial order, while the MFA results can be recovered at any time simply by considering $N_c\to\infty$. Finally, note that the OPT has the same spirit as the Hartree and Hartree-Fock approximation in which one also adds and subtracts a mass term. However, within these two traditional approximations, the topology of the dressing is fixed from the start: direct (tadpole) terms for Hartree and direct plus exchange terms for Hartree-Fock. On the other hand, within the OPT, $\bar\eta$ acquires characteristics which change order by order, progressively incorporating direct, exchange, vertex corrections, etc., effects. The OPT convergence within critical scalar theories has been proved in Ref. [25], but so far, no direct proof exists for the NJL model. Nevertheless, some important OPT results observed in the related four-fermion theory described by the Gross-Neveu model are encouraging for the present NJL application. Namely, in the $1+1$-dimensional Gross-Neveu model, the OPT improves over the large-N approximation by predicting smaller T_c values [41] in accordance with Landau's theorem for phase transitions in one space dimension, and in $2+1$ dimensions the OPT results point toward the Monte Carlo estimates [26].

To implement the OPT within the NJL model, one follows the prescription used in Refs. [26,30,41] by first interpolating the original four-fermion version. Then, in terms of the auxiliary fields, the deformed Lagrangian density becomes

$$\begin{aligned}\mathcal{L}=\bar\psi[i\gamma_\mu\partial^\mu-m_c-\delta(\sigma+i\gamma_5\boldsymbol{\tau}\cdot\boldsymbol{\pi})\\ -\eta(1-\delta)]\psi-\delta\frac{N_c}{2\lambda}(\sigma^2+\boldsymbol{\pi}^2),\end{aligned} \tag{3.4}$$

which shows that the Yukawa vertices have weight δ, while the meson "propagators" are proportional to $1/\delta$. One is then ready to perform a *perturbative* evaluation of Landau's free energy in powers of δ. In the σ direction, for the first nontrivial order, the relevant contributions are represented in Fig. 8. Then, at finite temperature and finite chemical potential, the order-δ result for the NJL free energy density is (see Ref. [30] for a more detailed discussion)

$$\begin{aligned}U_{\rm eff}(\sigma)=&\frac{\sigma^2}{4G}-2N_{\rm f}N_cI_1(\mu,T)\\ &+2\delta N_{\rm f}N_c(\eta+m_c)(\eta-\sigma)I_2(\mu,T)\\ &+4\delta GN_{\rm f}N_c\,I_3^2(\mu,T)\\ &-2\delta GN_{\rm f}N_c(\eta+m_c)^2I_2^2(\mu,T),\end{aligned} \tag{3.5}$$

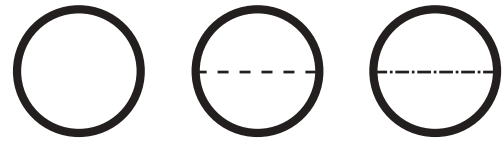

FIG. 8. Diagrams contributing to $U_{\rm eff}(\hat\eta)$ to order δ. The thick continuous fermionic lines represent $\hat\eta=m_c+\eta-\delta(\eta-\sigma)$ dependent terms which must be further expanded. The dashed lines represent the σ propagator, and the π propagator is represented by dashed-dotted line. The first contributes with $1/N_c^0$, the second and third diagrams (of order δ) contribute with $1/N_c$.

where we have replaced $\lambda\to 2GN_c$. In the above equation we have defined, for convenience, the following basic relevant integrals:

$$\begin{aligned}I_1(\mu,T)=\int\frac{d^3p}{(2\pi)^3}\{\varepsilon+T\ln[1+e^{-(\varepsilon+\mu)/T}]\\ +T\ln[1+e^{-(\varepsilon-\mu)/T}]\},\end{aligned} \tag{3.6}$$

$$I_2(\mu,T)=\int\frac{d^3p}{(2\pi)^3}\frac{1}{\varepsilon}\left[1-\frac{1}{e^{(\varepsilon+\mu)/T}+1}-\frac{1}{e^{(\varepsilon-\mu)/T}+1}\right], \tag{3.7}$$

and

$$I_3(\mu,T)=\int\frac{d^3p}{(2\pi)^3}\left[\frac{1}{e^{(\varepsilon-\mu)/T}+1}-\frac{1}{e^{(\varepsilon+\mu)/T}+1}\right], \tag{3.8}$$

where $\varepsilon^2=\mathbf{p}^2+(\eta+m_c)^2$. Notice also that I_3 only survives at $\mu\neq 0$. Here, we impose a sharp noncovariant cutoff Λ only for the vacuum term, since the finite temperature has a natural cutoff in itself specified by the temperature. This choice of regularization, which allows the Stefan-Boltzmann limit to be reproduced at high temperatures, is sometimes preferred in the literature [11,30,42]. Moreover, in the present application, it ensures that the temperature integrals appearing in the LσM and in the NJL are integrated over the same momentum range. Also, as will be further discussed, this regularization choice appears to be a crucial condition in order for the NJL model to reproduce the phase diagram with two critical points.

The divergent integrals occurring at $T=0$ and $\mu=0$ are

$$\begin{aligned}I_1(0,0)=&\int\frac{d^3p}{(2\pi)^3}\varepsilon\\ =&\frac{1}{32\pi^2}\left\{(\eta+m_c)^4\ln\left[\frac{[\Lambda+\sqrt{\Lambda^2+(\eta+m_c)^2}]^2}{(\eta+m_c)^2}\right]\right.\\ &\left.-2\sqrt{\Lambda^2+(\eta+m_c)^2}[2\Lambda^3+\Lambda(\eta+m_c)^2]\right\},\end{aligned} \tag{3.9}$$

and

$$\begin{aligned}I_2(0,0)=\int\frac{d^3p}{(2\pi)^3}\frac{1}{\varepsilon}=&\frac{1}{4\pi^2}\left\{\Lambda\sqrt{\Lambda^2+(\eta+m_c)^2}\right.\\ &\left.-\frac{(\eta+m_c)^2}{2}\ln\left[\frac{[\Lambda+\sqrt{\Lambda^2+(\eta+m_c)^2}]^2}{(\eta+m_c)^2}\right]\right\}.\end{aligned} \tag{3.10}$$

If needed, the $T \to 0$ limit of those integrals can be readily obtained (see Ref. [30]). Then, by applying the PMS relation to $U_{\rm eff}$, one gets

$$\left\{[\eta - \sigma - 2(\eta + m_c)GI_2]\left[1 + (\eta + m_c)\frac{d}{d\eta}\right]I_2 + 4GI_3\frac{d}{d\eta}I_3\right\}_{\eta=\bar{\eta}} = 0. \tag{3.11}$$

Notice that if one ignores the terms proportional to G (which are of order $1/N_c$), the optimal result is simply $\bar{\eta} = \sigma$. In this situation, Eq. (3.5) shows that the MFA result is exactly reproduced. Since we are mainly interested in the thermodynamics, one basic quantity of interest is the thermodynamical potential Ω, whose relation to the free energy is given by $\Omega = U_{\rm eff}(\bar{\sigma})$. The order parameter $\bar{\sigma}$ is determined from the gap equation generated by minimizing $U_{\rm eff}$ with respect to σ. From Eq. (3.5) we obtain [30]

$$\bar{\sigma} = 4GN_{\rm f}N_c(\eta + m_c)I_2. \tag{3.12}$$

To further discuss the relation of some of our results with those obtained by Fukushima [11], it is interesting to note, at this stage, that since $\bar{\sigma} = \langle\sigma\rangle = -2G\langle\bar{\psi}\psi\rangle = -2G\rho_s$ one can write the optimum thermodynamical potential as

$$\Omega = G\rho_s^2 + \Omega_{\rm MFAL}(\bar{\eta}) - (\bar{\eta} + 2G\rho_s)\rho_s + \frac{G}{N_cN_f}\left(\rho_q^2 - \frac{\rho_s^2}{2}\right), \tag{3.13}$$

where $\Omega_{\rm MFAL}(\bar{\eta})$ has the mathematical structure of a MFA-like thermodynamical potential whose effective mass is given by $\bar{\eta}$. Since $\Omega = -P$, one sees that the OPT introduces a correction like $-G/(N_cN_f)\rho_q^2$, which, although suppressed by $1/N_c$, is of the same form as the one considered by the MFA when a vector interaction term like $-G_V\bar{\psi}V\gamma_\mu V^\mu\psi$, as proposed in Ref. [31], is added to the original NJL Lagrangian density. When $N_c \to \infty$, $\bar{\eta} = -2G\rho_s$ and the MFA result (for the standard NJL model) with no ρ_q dependence is recovered.

B. Nonstandard parametrization and the appearance of two critical points

Usually, the three NJL parameters, G, m_c, and Λ, are fixed by fitting the pion decay constant $f_\pi = 92.4$ MeV, the quark condensate $190 \lesssim -\langle\bar{\psi}\psi\rangle^{1/3} \lesssim 260$ MeV as well as the pion mass $m_\pi = 135$ MeV, leading, in the MFA, to values such as $\Lambda = 664.3$ MeV, $G\Lambda^2 = 2.06$, and $m_c = 5$ MeV [39]. With these values, one obtains satisfactory predictions for the quark vacuum effective mass m_q^0 and for the quark condensate $\langle\bar{\psi}\psi\rangle$ given by $m_q^0 = 300$MeV and $-\langle\bar{\psi}\psi\rangle^{1/3} = 250.8$ MeV. Although in general the noncovariant cutoff lies within the range 500–700 MeV while $m_c \sim 5$ MeV, the coupling can be further increased producing much higher values for m_q^0 without affecting too much the G independent quark condensate. For example, another MFA set also presented in Ref. [39] is given by $\Lambda = 568.6$MeV, $G\Lambda^2 = 3.17$, and $m_c = 5.1$ MeV, predicting $m_q^0 = 600$MeV $> \Lambda$ and $\langle\bar{\psi}\psi\rangle = -247.5$ MeV. As one can see, the value of m_q^0 doubles while that of the observable $\langle\bar{\psi}\psi\rangle$ remains within the bounds 190 MeV $\lesssim -\langle\bar{\psi}\psi\rangle^{1/3} \lesssim 260$ MeV set by sum rules [43] and the value $-\langle\bar{\psi}\psi\rangle^{1/3} \simeq 231$ MeV which corresponds to lattice estimates [44]. Regarding applications at finite temperature and density, one sees that also the values of the critical temperature (at $\mu = 0$) and of the critical chemical potential (at $T = 0$) increase with G. In general, the size of the first-order transition line, which originates at high $\mu(\sim m_q^0)$ and $T = 0$, increases with G approaching the T axis for very high coupling strengths. This observation, together with the LσM results that the appearance of two critical points becomes possible for $m_\pi < 50$ MeV gives us the hint to use the OPT at high G and small m_c (since $m_\pi \propto m_c$) while setting Λ to usual values. For consistency we must use the OPT two-loop relations for f_π and m_π recently found in Ref. [30] and which predict some deviations from the MFA result for the Gell–Mann-Oakes-Renner relation. Taking $\Lambda = 590$ MeV, and $G\Lambda^2 = 3.7$ with $m_c = 4.5$ MeV, one obtains the very reasonable values $f_\pi \simeq 92$ MeV, $m_\pi \simeq 135$ MeV, and $-\langle\bar{\psi}\psi\rangle^{1/3} \simeq 264$ MeV. However, now G has an extremely high value which is reflected in the vacuum effective quark mass value, $m_q^0 \simeq 787$ MeV. Next, one can keep those values of Λ and G, decreasing m_c so as to make contact with the LσM results. For example, $m_c = 0.1$, 0.28, and 0.55 MeV lead to $m_\pi = 20$, 35, and 50 MeV, while f_π and $\langle\bar{\psi}\psi\rangle^{1/3}$ remain very stable. With this aim, let us analyze the phase transition pattern at high T and $\mu = 0$ in search for a first-order transition, taking $m_c = 0.1$ MeV (with $\Lambda = 590$ MeV and $G\Lambda^2 = 3.7$). Within the OPT this choice predicts $f_\pi \simeq 92.2$ MeV, $m_\pi \simeq 20$ MeV, and $-\langle\bar{\psi}\psi\rangle^{1/3} \simeq 263$ MeV with the expected high quark mass value, $m_q^0 = 781$ MeV. In principle, one could object to the fact that $m_q^0 > \Lambda$ (apart from having a numerical value much higher

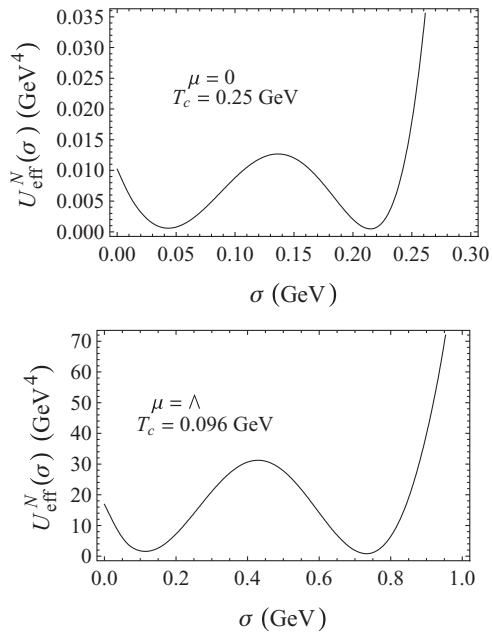

FIG. 9. Normalized free energy, $U_{\rm eff}{}^N(\sigma) = [U_{\rm eff}(\sigma) - U_{\rm eff}(\bar{\sigma})] \times 10^{-7}$, as a function of σ for ($\mu = 0$ MeV, $T_c = 0.25$ GeV) (top panel) and ($\mu = \Lambda$, $T_c = 0.096$ GeV) (bottom panel), showing first-order phase transition.

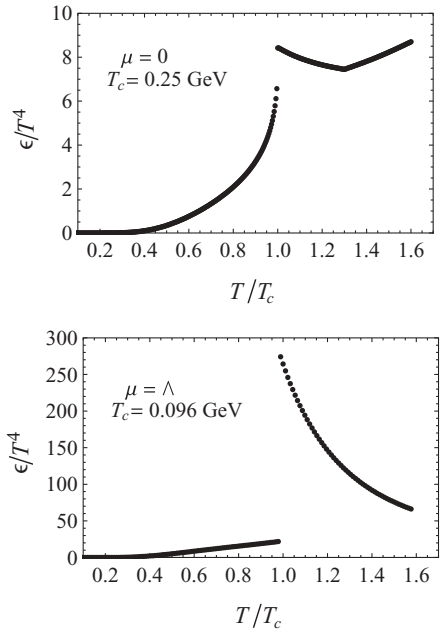

FIG. 10. ϵ/T^4 vs T/T_c for $\mu = 0$, $T_c = 250$ MeV (top panel) and $\mu = \Lambda = 590$ MeV, $T_c = 96$ MeV (bottom panel). The associated latent heat is $\Delta\epsilon = 0.3 \times 10^{-2}$ GeV^4 for the top panel and $\Delta\epsilon = 1.72 \times 10^{-2}$ GeV^4 for the bottom panel. In both cases, $G\Lambda^2 = 3.7$ and $m_c = 0.1$.

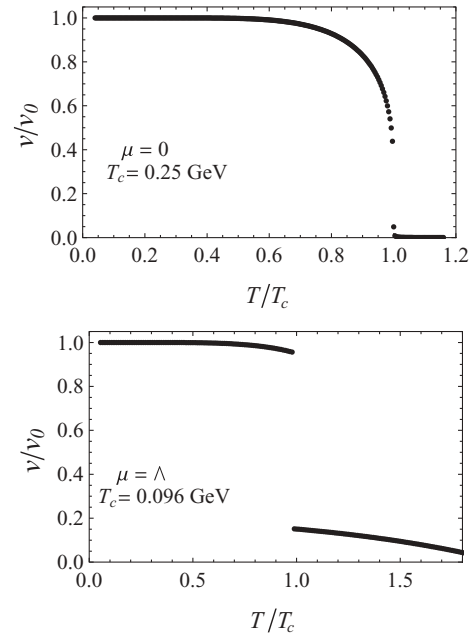

FIG. 11. Dimensionless quark condensate ratio v/v_0 vs T/T_c for $\mu = 0$, $T_c = 250$ MeV (top panel) and $\mu = \Lambda = 590$ MeV, $T_c = 96$ MeV (bottom panel). In both cases, $G\Lambda^2 = 3.7$ and $m_c = 0.1$.

than 1/3 of the baryonic mass). However, the large value of G mostly affects m_q^0, which is a bare parameter apart from being unphysical, while physical observables such as f_π, m_π, and $\langle\bar{\psi}\psi\rangle^{1/3}$ remain realistic.

With these unusual parameter values, one indeed obtains a first-order transition at $\mu = 0$ and $T = 0.25$ GeV, as shown by the top panel of Fig. 9, while the usual first-order transition is also observed at $T = 0$ and $\mu_c \simeq 680$MeV $< m_q^0$ starting a line of first-order transitions, as shown by the bottom panel of Fig. 9, which shows the degenerate minima at $\mu = \Lambda$ and $T = 0.096$ GeV.

The differences in latent heat, $\Delta\epsilon$, between the two transitions can be further observed by looking at Fig. 10, which shows the normalized ϵ/T^4 versus the dimensionless ratio T/T_c. The values are $\Delta\epsilon = 0.3 \times 10^{-2}$ GeV^4 for $\mu = 0$ and $T = 250$ MeV and $\Delta\epsilon = 1.72 \times 10^{-2}$ GeV^4 for $\mu = \Lambda$ and $T = 96$ MeV (and of course higher for $T = 0$, $\mu = 680$ MeV, but we shall refrain from numerically exploring the $\mu > \Lambda$ region).

The situation can be also observed by analyzing the thermal behavior of the order parameter represented by the quark condensate $v = \langle\bar{\psi}\psi\rangle$, which is given in Fig. 11 for $\mu = 0$ and $\mu = \Lambda$. This figure clearly indicates that the first order happening at high T and vanishing $\mu = 0$ is much softer than the one happening in the reversed situation of small T and high μ, a fact which is well illustrated by the three-dimensional plot of Fig. 12, which already shows that these two first-order transition lines are indeed separated by a crossover region at intermediate T and μ.

This fact can be more clearly appreciated by projecting the first-order lines of Fig. 12 on the T-μ plane as in Fig. 13.

This phase diagram is qualitatively very similar to the one obtained in Fig. 2 for the LσM (as mentioned above, our value $m_c = 0.1$ leads to $m_\pi = 20$ MeV) and constitutes our first important result concerning the NJL model. Namely, that by going beyond the MFA and choosing the parameters so as to reproduce small pion masses, one may obtain a second critical end point in the phase diagram. In addition, the choice of regularization procedure appears to be crucial to the appearance of c_1 in the NJL model. If one uses a cut off also in the T dependent integrals the critical point c_1 does not emerge. However, some authors (see Ref. [42]) have recognized that a three-dimensional cutoff is only needed at zero temperature, since the presence of high-momentum quarks in the T-dependent Feynman loops is required to ensure that the entropy density scales as T^3 at high temperature. Here, we have found that in the limit of a very strong coupling and

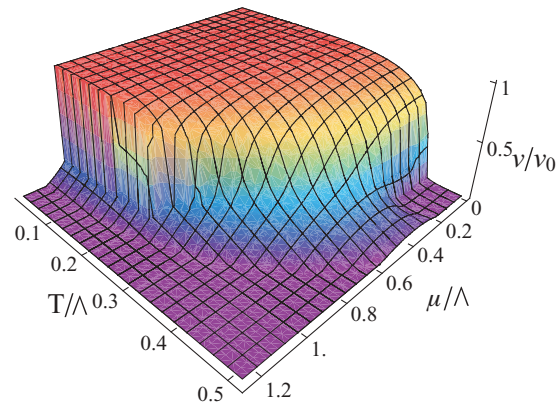

FIG. 12. (Color online) Dimensionless quark condensate ratio v/v_0 as a function of T/Λ and μ/Λ.

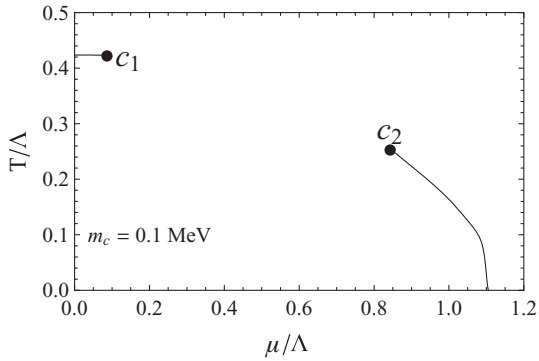

FIG. 13. Phase diagram in the T-μ plane for $m_c = 0.1$ MeV ($m_\pi \simeq 20$ MeV) and corresponding to the choice $G\Lambda^2 = 3.7$.

small current mass, which induces high $T_c(\mu = 0) \sim 0.4\Lambda$, the upper limit of the thermal integral, given by Λ/T, seems to wash out important thermal contributions which induce the rather subtle first-order transition. That is, it seems that the appearance of a critical point at high T can only be achieved when a regularization which reproduces the Stefan-Boltzmann limit is adopted. On the other hand, only the T-μ plane location of the usual critical point (small T and high μ) is influenced by the regularization choice. In contrast, by being renormalizable, the LσM always allows for high-momentum quarks in the T-dependent loops. Therefore, with our regularization choice, the temperature-dependent integrals within the NJL are treated on the same footing as their LσM counterparts. A comprehensive discussion about how parameters and regularization affect NJL has recently been carried out by Costa *et al.* [42]. For our parameter values, the location of c_1 happens at the point ($T_{c_1} = 249.75$ MeV, $\mu_{c_1} = 51.16$ MeV) and of c_2 at the point ($T_{c_2} = 149.78$ MeV, $\mu_{c_2} = 497.55$ MeV). From the quantitative point of view, these values are high, as one would expect from the fact that m_q^0 is also high. Note also how the first-order line associated with c_1 is almost parallel to the μ axis.

The next step is to understand the physical nature of both critical first-order lines. Our study of the susceptibilities and densities in the LσM has revealed that the high-T small-μ line terminating at c_1 has a more "chiral" character, while the small-T and high-μ line terminating at c_2 has a more hydrodynamical character. One can then map the T-μ points to form a phase coexistence diagram such as the T versus ρ_B/ρ_0 shown in Fig. 14, where $\rho_0 = 0.17$ fm^{-3} is the normal nuclear density. The top figure shows that the coexistence region associated with the traditional c_2 point goes from $T = 0$ to $T = 149.78$ MeV, covering very high baryonic densities. The unusual region, on the other hand, is very tiny going from $\rho_B = 0$ to $\rho_B = 0.85\rho_0$, being restricted to a very narrow temperature range as shown by the bottom panel. The critical points c_1 and c_2 are located at $\rho_B = 0.95\rho_0$ and $\rho_B = 4\rho_0$, respectively.

At $\rho_B = 0$, the small coexistence region terminates into a point located at $T = 250$ MeV. Both coexistence regions have very different shapes, especially near the critical points, from which one may expect that the associated critical exponent β, to be evaluated later, acquires different values in each situation. Let us now map the T-μ results into the P-ρ_0/ρ_B plane as shown by Fig. 15, which, again, clearly indicates that the region associated with c_2 in fact looks like the mixed liquid-gas phase

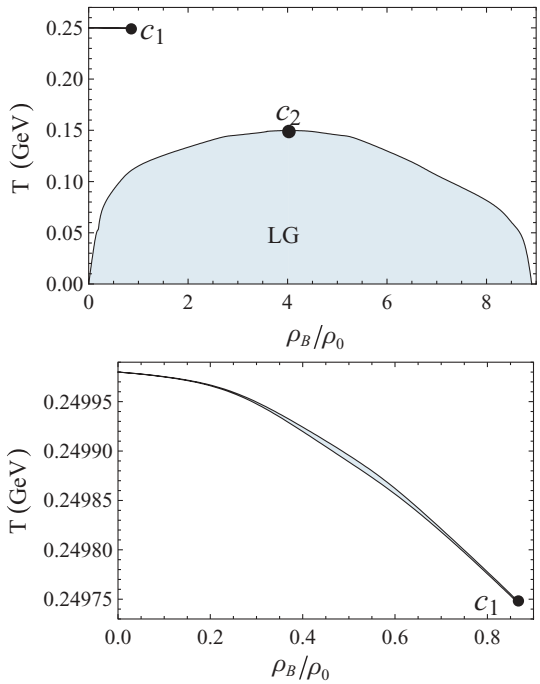

FIG. 14. (Color online) Phase coexistence diagram in the T-ρ_B/ρ_0 plane, where $\rho_B = \rho/3$ is the baryonic density and $\rho_0 = 0.17$ fm^{-3} is the nuclear matter density. Here, $m_c = 0.1$ MeV, predicting $m_\pi \simeq 20$ MeV with the choice $G\Lambda^2 = 3.7$. The two dark regions denote a mixed phase with LG denoting the liquid-gas type. The bottom panel is an expanded view of the phase coexistence region associated with the high-T first-order transition line.

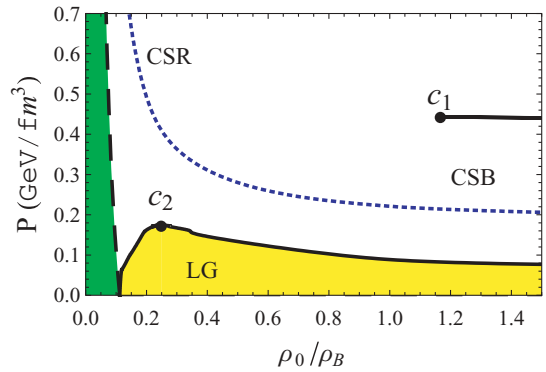

FIG. 15. (Color online) Phase diagram in the P-ρ_0/ρ_B plane, where $\rho_B = \rho/3$ is the baryonic density and $\rho_0 = 0.17$ fm^{-3} is the nuclear matter density. Here $m_c = 0$ (chiral limit), and CSB represents the broken phase ("gas"), while CSR represents symmetric phase ("liquid"). The long dashed line is the $T = 0$ isothermal, and the dark region to its left is not accessible. The short dashed line represents the $T = 220$ MeV isothermal corresponding to a crossover temperature. The large mixed phase corresponding to the usual first-order transition line of the liquid-gas (LG) type is labeled, the dot marks c_2. The thick continuous line at $P \simeq 0.45$ GeV/fm^3 represents the region associated with the unusual line, and the dot marks c_1.

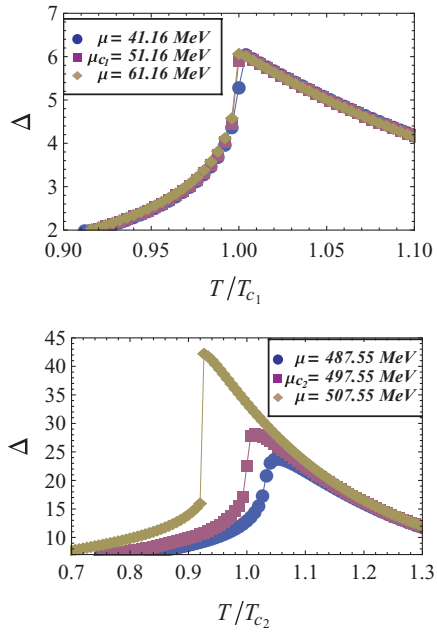

FIG. 16. (Color online) Interaction measure Δ for the critical points c_1 (top panel) and c_2 (bottom panel). Chemical potentials above and below the critical point values are also shown for reference. In both cases, $G\Lambda^2 = 3.7$ and $m_c = 0.1$.

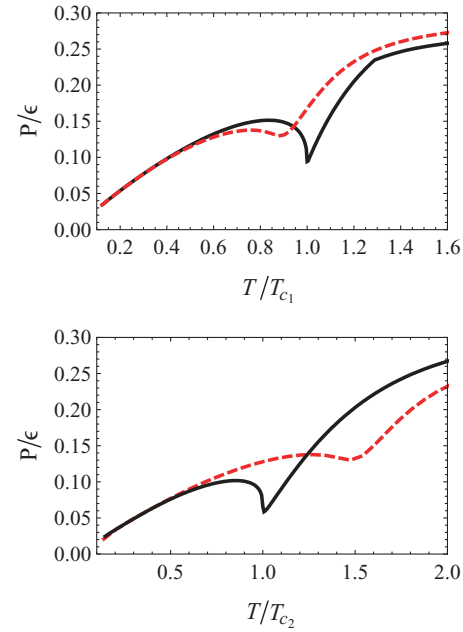

FIG. 17. (Color online) EOS parameter $w = P/\epsilon$ vs temperature for the critical points c_1 (continuous line, top panel) and c_2 (continuous line, bottom panel). In both cases, $G\Lambda^2 = 3.7$ and $m_c = 0.1$. For reference, we show the EOS parameter for $\mu > \mu_{c_1}$ (dashed line, top panel) and $\mu < \mu_{c_2}$ (dashed line, bottom panel). Here, $G\Lambda^2 = 3.7$ and $m_c = 0.1$.

appearing in the P-V type of phase diagram for a van der Waals fluid (which does not contain a phase analogous to the mixed phase associated with c_1).

C. Thermodynamical quantities near the critical points

The OPT result for $\Omega = -P$ allows us to obtain $\epsilon = -P + Ts + \mu\rho_q$ for the NJL with the inclusion of finite $1/N_c$ corrections, which makes it possible to analyze the critical behavior near each of the two critical points. With this aim we will numerically evaluate the following thermodynamical quantities: the interaction measure (or trace anomaly, Δ), the equation-of-state (EOS) parameter ($w = P/\epsilon$), the bulk viscosity over entropy density (ζ/s), the quark number and chiral susceptibilities (χ_q and χ_m) as well as some critical exponents. Let us start by considering the interaction measure

$$\Delta = \frac{\epsilon - 3P}{T^4}, \tag{3.14}$$

which is plotted in Fig. 16 for regions near c_1 and c_2. This quantity is expected to peak near a phase transition or crossover and can be helpful in locating the critical line. Figure 16 indicates that the rise near c_1 looks more uniform around c_2 and happens for temperatures near T_{c_1}, which is not surprising since there is little variation in T along the associated first-order line as already emphasized. Although the peaks associated with c_2 look more pronounced, one has to recall that Δ is normalized by $1/T^4$ and that the c_2 region is associated with lower temperatures.

Next, let us investigate the EOS parameter w, as represented by Fig. 17 for the two critical points. In both situations, one observes a downward cusp at the critical temperatures (very much like in the case of the squared speed of sound, $V_s^2 = dP/d\epsilon$). Below the critical temperature, our results show a bump which is also observed in the usual LσM, Polyakov LσM, and lattice studies (see Ref. [45]). For high values of T, the quantity $w = P/\epsilon$ converges to approximately $1/3$, as expected.

The bulk viscosity ζ is an intrinsic dynamical quantity which, however, can be expressed in terms of the static thermodynamical quantities derived from the free energy as [46]

$$\zeta = \frac{1}{9\omega_0}\left[T^5 \frac{\partial}{\partial T}\frac{(\epsilon - 3P)}{T^4} + 16|\epsilon_0|\right], \tag{3.15}$$

where ω_0 is a scale which will be set to Λ, as in Ref. [30], while ϵ_0 represents the vacuum part of the energy density. Since ζ is proportional to the specific heat C_v, the bulk viscosity over entropy density, ζ/s, behaves as $1/V_s^2$ near T_c in this approximation and peaks at the critical end points, as indeed shown by our Fig. 18, where the divergences at (T_{c_1}, μ_{c_1}) and at (T_{c_2}, μ_{c_2}) indicate that the energy density has a sudden change at the critical points typical of a first-order transition. For our purposes, this is an interesting quantity since it has been pointed out that one can distinguish whether the system experiences a first-order phase transition or a crossover from observables which are sensitive to the bulk viscosity in experiments like those performed at the BNL Relativistic Heavy Ion Collider. One expects that a sharp rise of bulk viscosity near a phase transition induces an instability in the hydrodynamic flow of the plasma, and this mode will blow up, tearing the system into droplets [45].

Let us now examine numerically the behavior of the quark susceptibility χ_q, as well as of the chiral susceptibility χ_m,

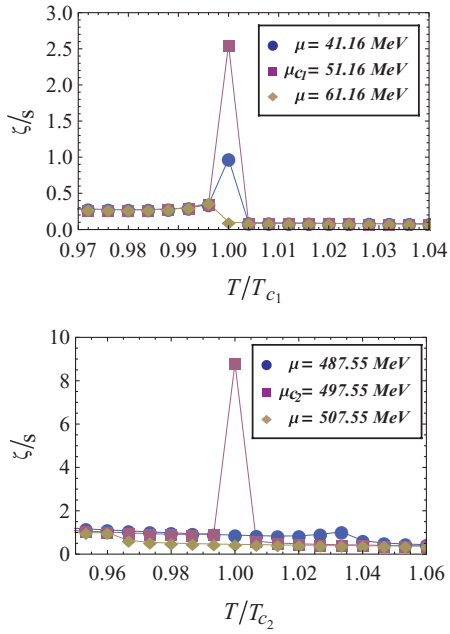

FIG. 18. (Color online) Bulk viscosity over entropy density, ζ/s, as a function of temperature for the critical points c_1 (top panel) and c_2 (bottom panel). Chemical potential above and below the critical point values are also shown for reference. Here, $G\Lambda^2 = 3.7$ and $m_c = 0.1$.

near the two critical points. These quantities are, respectively, given by

$$\chi_q = \frac{\partial \rho_q}{\partial \mu}, \tag{3.16}$$

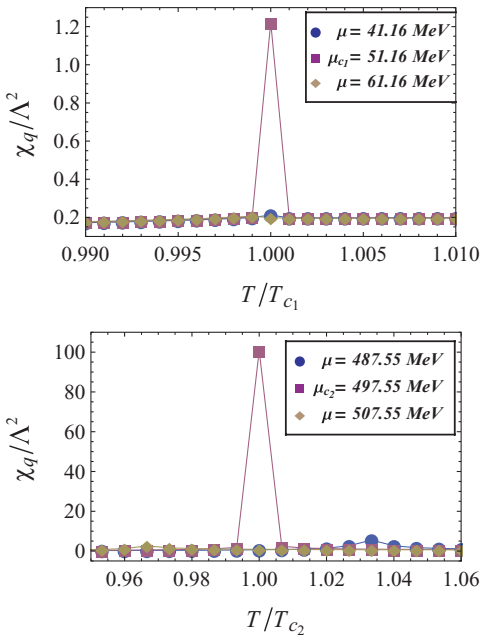

FIG. 19. (Color online) Normalized quark susceptibility, χ_q/Λ^2, for the critical points c_1 (top panel) and c_2 (bottom panel). Chemical potentials above and below the critical point values are also shown for reference. Here, $G\Lambda^2 = 3.7$ and $m_c = 0.1$.

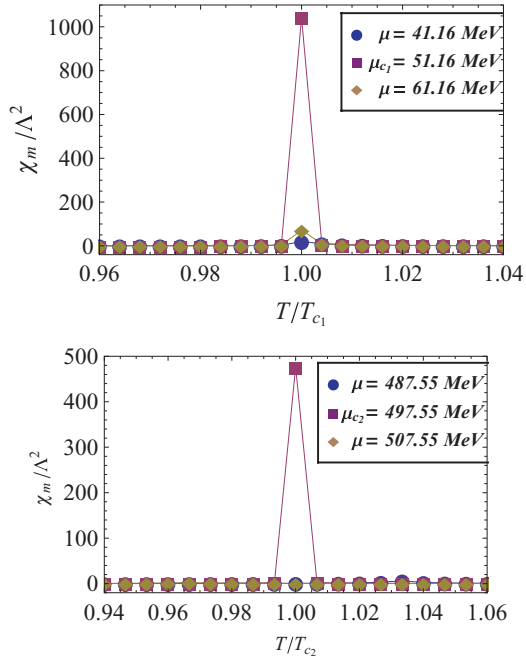

FIG. 20. (Color online) Normalized chiral susceptibility, χ_m/Λ^2, for the critical points c_1 (top panel) and c_2 (bottom panel). Chemical potentials above and below the critical point values are also shown for reference. Here, $G\Lambda^2 = 3.7$ and $m_c = 0.1$.

and

$$\chi_m = \frac{\partial \rho_s}{\partial m_c}. \tag{3.17}$$

Figures 19 and 20 show χ_q and χ_m, respectively, as functions of T for relevant values of μ. As expected, one observes that these two quantities peak for both c_1 and c_2. However, for χ_q, the magnitude of the peak associated with c_2 seems to be much larger, while for χ_m the difference is not so dramatic. In principle these results could be interpreted as showing that the quark density ρ_q plays a very minor role within c_1, while ρ_s seems to dominate that critical point. At the same time, the liquid-gas type of critical point, c_2, seems to receive contributions from both types of density in accordance with our results for the LσM.

These findings can be further appreciated if one investigates free energy in terms of the two ordering densities, ρ_s and ρ_q, by using the techniques of Fujii and Ohtani [47] to Legendre transform $U_{\rm eff}(T, \mu, m_c)$ to $\mathcal{V}_{\rm eff}(T, \mu, m_c; \rho_s, \rho_q)$. The result of this type of manipulation is shown in Fig. 21 for the two critical points c_1 and c_2, as well as at an intermediate point ($T = 240$ MeV, $\mu = 150$ MeV) where a crossover takes place. The contour plots displayed by Fig. 21 indicate that c_1 is indeed dominated by the scalar interaction ρ_s, while the quark (vector) density also plays an important role at c_2 in accordance with the covariance matrix results for the LσM.

Finally, the data used in the coexistence phase diagram T-ρ_B allow us to evaluate the critical exponent β defined as $|\rho_q^+ - \rho_q^-| \propto |T - T_E|^\beta$, where E represents c_1 or c_2, while ρ_q^+ and ρ_q^- represent the two corresponding densities for a given temperature. Having the quark number susceptibility allows the numerical evaluation of the critical exponent ϵ, $\chi_q \propto$

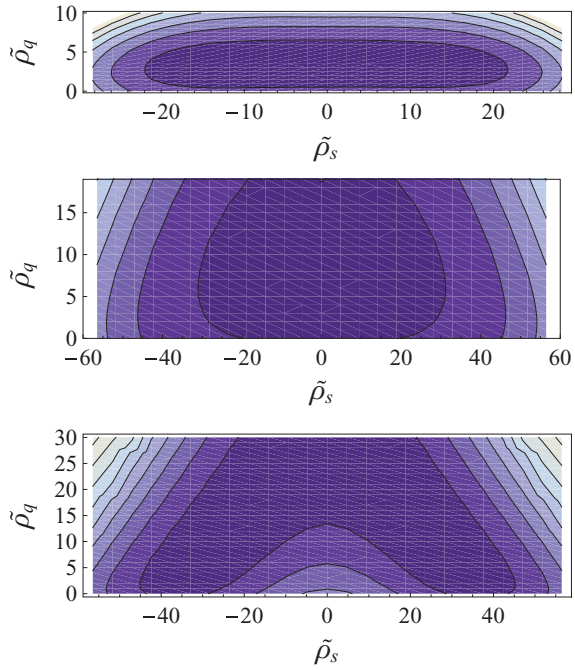

FIG. 21. (Color online) Legendre-transformed effective potential $\mathcal{V}_{\text{eff}}(T, \mu, m_c; \rho_s, \rho_q)$ projected in the dimensionless plane $\tilde{\rho}_s$-$\tilde{\rho}_q$ plane, where $\tilde{\rho} = \rho/(10^6\ \text{MeV}^3)$ in both cases. The top panel shows this quantity at c_1, the middle panel shows it at $T = 240$ MeV, $\mu = 150$ MeV, where a crossover takes place. The bottom panel shows the contour plot at c_2.

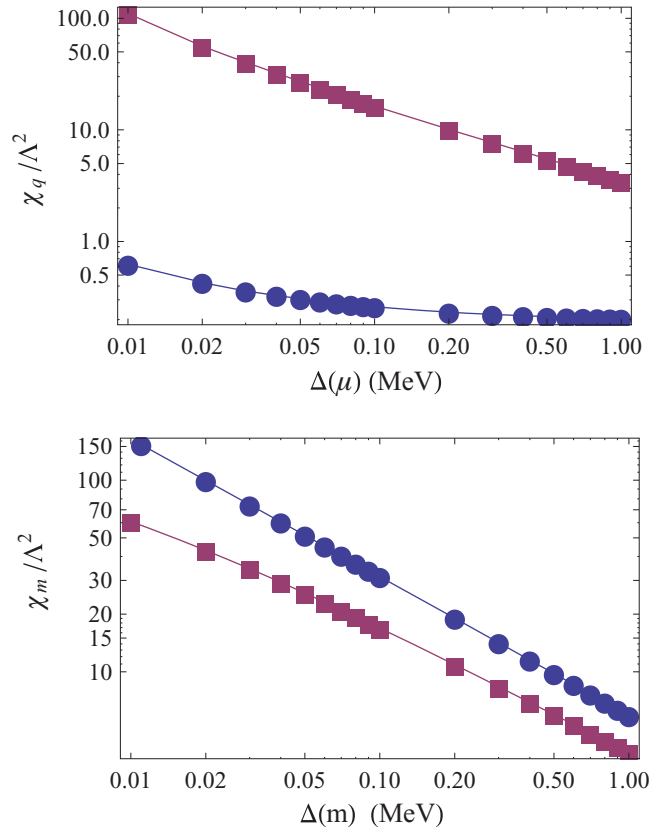

FIG. 22. (Color online) Top panel: Logarithmic plot of the dimensionless χ_q/Λ^2 as a function of $\Delta(\mu) = |\mu - \mu_{c_2(c_1)}|$ approached from $\mu < \mu_{c_2(c_1)}$. The dots correspond to c_1 and the squares to c_2. Bottom panel: Same type of plot for the dimensionless χ_m/Λ^2 as a function of $\Delta(m) = |m - m_c|$ approached from $m > m_c$.

$|\mu - \mu_E|^{-\epsilon}$, for which one may define a chiral counterpart ϵ_m, given by $\chi_m = |m_c - m|^{-\epsilon_m}$. This procedure is illustrated by the top panel of Fig. 22, in which ϵ is obtained by approaching the critical point in a path parallel to the μ axis from $\mu < \mu_{c_1(c_2)}$. The value $\epsilon \simeq 0.64$ for c_2 is close to the one obtained in Ref. [48] while for c_1 the value is $\epsilon \simeq 0.50$. The bottom panel of Fig. 22 shows the same procedure for ϵ_m with the critical points being approached from the m "wing" of the T-μ plane, with $m > m_c$. Interestingly enough, the numerical values get approximately inverted, when compared to ϵ, and one gets $\epsilon_m \simeq 0.49$ for c_2 and $\epsilon_m \simeq 0.63$ for c_1. A similar type of procedure gives $\beta \simeq 0.48$ for c_1 and $\beta \simeq 0.35$ for c_2. Having β and ϵ allows us to determine δ, γ, and α using $\epsilon = 1 - 1/\delta$, $\gamma = \beta(\delta - 1)$, and $\alpha + 2\beta + \gamma = 2$. The values for the remaining exponents have been obtained after approximating our numbers for β and ϵ by the ratios shown in Table I. Note that although our numerical estimates are very crude, since we do not cover many orders of magnitude nor try possible different paths leading to the critical points, they support our previous discussion regarding the nature of the two critical points found in this work. In particular, the values for β listed in Table I support the liquid-gas character of c_2 [49]. For this critical point also, the exponent ϵ, associated with χ_q, is greater than the one for the critical point c_1. Note also that the values of α obtained by using our approximate ratios for β and ϵ in the scaling relations show that $\alpha = \epsilon$ for both critical points, which is consistent with the universal arguments presented in Refs. [10,50] since it is expected that χ_q and C_v should be the same near the critical points. A detailed and highly precise determination of the associated critical exponents is beyond the scope of the present application, and the interested reader is referred to Refs. [10,42,48].

D. Back-bending in the μ-m_c plane

It will be interesting to explicitly show that, at least from a qualitative perspective, our model predictions can be relevant for the lattice results obtained by de Forcrand and Philipsen [16] who observed a shrinkage of the first-order transition region when considering higher values of μ. For completeness, let us also compare the OPT with the MFA results when the model parameters are tuned so that the latter approximation also generates a first-order transition at $\mu = 0$. Within the NJL model, the MFA can predict a

TABLE I. Approximate ratios for the critical exponents associated with c_1 and c_2 in the NJL model. The values in parentheses are the results which have been numerically obtained.

CEP	α	β	γ	δ	ϵ	ϵ_m
c_1	1/2	1/2 (0.48)	1/2	2	1/2 (0.50)	2/3 (0.63)
c_2	2/3	1/3 (0.35)	2/3	3	2/3 (0.64)	1/2 (0.49)

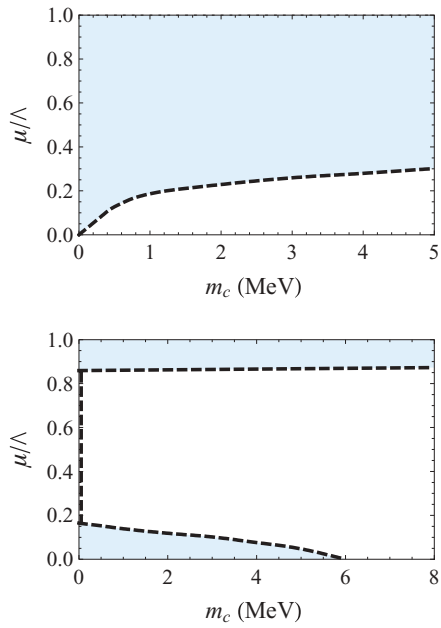

FIG. 23. (Color online) μ vs m_c plane showing the second-order transition boundary (dashed lines) associated with the critical point(s) for the NJL. The shadowed regions correspond to first-order transitions, and the white areas represent the crossover regions. The top panel corresponds to MFT and shows only a single first-order branch with one critical point. The bottom panel corresponds to OPT and shows the possibility of two first-order branches associated with two distinct critical points. Both results are for $G\Lambda^2 = 3.98$.

first-order transition at $\mu = 0$ and for $\Lambda = 590$ MeV when the higher coupling, $G\Lambda^2 = 3.98$, is used with $m_c = 0.1$ MeV. In this case, the MFA also predicts $f_\pi \simeq 93$ MeV, $m_\pi \simeq 20$ MeV, and $-\langle\bar{\psi}\psi\rangle^{1/3} \simeq 263.5$ MeV, and $m_q^0 \simeq 814$ MeV while, for the same set of parameters, the OPT predicts $f_\pi \simeq 90.68$ MeV, $m_\pi \simeq 20.73$ MeV, and $-\langle\bar{\psi}\psi\rangle^{1/3} \simeq 265$ MeV, and $m_q^0 \simeq 856$ MeV.

In the μ -m_c plane, the NJL model then generates Fig. 23, in which the top panel, corresponding to the MFA, shows only a one-branch first-order line. When the OPT is applied to the NJL with the stronger $G\Lambda^2 = 3.98$ considered in this section, one observes a first-order line for $m_c < 3.5$ MeV which roughly corresponds to $m_\pi = 122$ MeV. Starting at the point $m_c = 3.5$ MeV, $\mu = 0$, one may follow a second-order transition line which goes left touching the μ axis at $\mu \simeq 70$ MeV and then going up to $\mu \simeq 350$ MeV where it bends back to the right-hand side for finite values of m_c. The situation is illustrated by the bottom panel of Fig. 23.

Therefore, when one goes beyond MFA, the NJL also predicts a bending-back behavior of the critical line in a way which is consistent with the negative curvature of the lattice simulations of Refs. [16]. This result also supports Fukushima's suggestion [11] regarding the eventual back bending. Although this author has considered the SU(3) version of the NJL (being able to reproduce a critical surface in the $m_{u,d}$-m_s-μ space) with standard parametrization, it is interesting to note that the bending was obtained by adding a vector interaction which generated a $-G_V\rho_q^2$ contribution to the pressure. By looking at our Eq. (3.13), one sees that the OPT also brings a term like $-G/(N_cN_f)\rho_q^2$ to $P = -\Omega$. Finally, note that a back-bending behavior is also implied by our LσM results if one considers that c_2 and c_2' almost coincide.

IV. CONCLUSIONS

In recent publications [12,13], it was shown that for small values of the vacuum pion mass ($\lesssim$50 MeV) the phase diagram of the LσM has two distinct first-order lines terminating in two critical points. One, as predicted by most models, starts at finite μ and $T = 0$, whereas the other is an unusual first-order line which starts at high T and $\mu = 0$. In between the critical endpoints (whose exact location depends on the vacuum pion mass) of these two lines, there is a crossover transition. At the origin of this behavior, which is not observed in the MFA, are the thermal fluctuations of the mesonic fields, which have been taken into account adopting a self-consistent method first proposed in Ref. [32]. Inspired by this finding, we have performed a careful analysis of the LσM with the aim of understanding in deeper detail the nature of the critical points. At the same time, we have considered another popular effective quark model, the NJL model, to investigate under which conditions a phase diagram with at least two distinct critical points could be reproduced.

The analysis of the LσM has been performed by using the same method of Ref. [12], and our results agree with the ones obtained therein: the unusual first-order line which starts at high T and $\mu = 0$ ending in the "new" critical point (c_1) was also found. At the same time, a closer look in the vicinity of the "usual" critical end point revealed that, right before the end, the first-order line that starts at finite μ and $T = 0$ bifurcates into *two* critical end points (c_2 and c_2') separated by a few MeV in T and μ.

In addition to the phase diagram, we have studied susceptibilities and correlations of the net-quark number density, the entropy density, and the scalar density. Our results for the covariant matrix show that for c_1 the dominant fluctuations are given by the scalar density and the entropy density, whereas the quark number density plays only a minor role. For the two critical points c_2 and c_2', instead, the fluctuations of the quark number density are also important. Their contribution becomes larger as the vacuum pion mass is increased, probably also due to the fact that c_2 and c_2' move toward higher values of μ. Despite their vicinity in the phase diagram, c_2 and c_2' seem to exhibit distinct features. The main difference is the fluctuation of the scalar density, which is more important in c_2' than in c_2.

We then considered the NJL thermodynamical potential, recently evaluated with the OPT [30], with parameter values which simulate small pion masses in order to generate a T-μ phase diagram in which the existence of two critical points, c_1 and c_2, separated by a crossover region has been observed. This type of phase diagram is similar to the one found, in the temperature-magnetic field plane, for the compressible metamagnetic Ising model [20].

We have performed an extensive thermodynamical analysis in order to find the essential physical features that distinguish both critical points, concluding, in agreement with the LσM case, that the usual one (c_2) located at intermediate values of

T and μ has a more hydrodynamical character, with the quark number density playing an essential role. This density has little influence at lower values of μ where the new, unusual, critical point c_1 region is dominated by the scalar density. Although we have not considered a vector term in the version of the NJL model considered here, it is rather interesting to note that the OPT pressure has the term $-G/(2N_f N_c)(2\rho_q^2 - \rho_s^2)$ which by being $1/N_c$ suppressed does not contribute to the MFA, which completely misses the possible existence of c_1 and the associated first-order line.

From these results, it is clear that the inclusion of contributions beyond MFA can have dramatic consequences on the phase diagram of quark models and cannot be neglected. With the combined analysis of the LσM and the NJL model, we have shown that the appearance of multiple critical points is not an uncommon feature of effective quark models, even without explicitly introducing a vector interaction as was done in Ref. [11].

Before exporting these notions to QCD, however, some caution is advisable. As has been very recently shown in Ref. [19], based on the analysis of the LσM in MFA, the inclusion of vacuum fluctuations can change the transition in the chiral limit at $\mu = 0$ from first to second order, so that this model would behave as the NJL model in the same regime. However, our results for the latter suggest that the consideration of vacuum contributions should not influence the appearance of the critical point c_1, at least qualitatively, when an appropriate tuning of model parameters is carried out beyond the MFA. In the minimal version of the NJL model considered here, c_1 appears only if the coupling is larger than usual (see discussion in Sec. III B), while a sharp cutoff is introduced only in the divergent integrals. However, having a large parameter space, more sophisticated versions of the model could also allow the appearance of a critical point like c_1 while generating more plausible values for the vacuum effective quark mass.

Concerning the other two critical points found in the LσM (c_2 and c_2'), instead, vacuum fermion loops are not expected to modify dramatically the qualitative behavior of the model, especially for values of the vacuum pion mass close to the physical one [32]. The presence of c_2' in the LσM with thermal fluctuations, however, has not been confirmed by the OPT analysis of the NJL model. This might be due to various reasons including the fact that the two models have been evaluated under different approximations, the fact that the NJL does not have true mesonic degrees of freedom, etc. The clarification of these points calls for further investigations.

Nevertheless, our results allow us to conclude that it is possible to use these effective models to generate metamagnetic-like phase diagrams at the expense of using nonstandard parameters for m_c and m_π which weakly break chiral symmetry in approximations which go beyond the MFA. Having two critical points, it then becomes possible to observe the shrinkage of the first-order region, in the μ-$m_c(m_\pi)$ plane, as one considers higher values of μ so that model predictions could be conciliated with the lattice results by de Forcrand and Philipsen [16]. Then, as we have shown, the first-order region should increase again, eventually intercepting the physical mass point as argued in Ref. [13]. The chiral-like first-order transition observed in the line associated with c_1 seems to be much softer and the coexistence regions much smaller than in the traditional liquid-gas type of line associated with c_2, which perhaps would make it harder to be detected in lattice QCD calculations (see, for example, Ref. [51]). Although quantities such as the trace anomaly, EOS parameter, bulk viscosity, and susceptibilities display the expected behavior associated with first-order phase transitions, it seems that the different critical points belong to distinct universality classes.

ACKNOWLEDGMENTS

M.B.P. thanks the Nuclear Theory Group at LBNL for the hospitality during the sabbatical year. We thank J.-L. Kneur, R. Ramos, I. N. Mishustin, W. Figueiredo, P. Costa, Y. Hatta, H. Hansen, and A. Delfino for discussions. This work was supported by the Director, Office of Energy Research, Office of High Energy and Nuclear Physics, Divisions of Nuclear Physics, of the US Department of Energy under Contract No. DE-AC02-05CH11231, by the Helmholtz International Center for FAIR within the framework of the LOEWE program (Landesoffensive zur Entwicklung Wissenschaftlich-Ökonomischer Exzellenz) launched by the State of Hesse, and by Coordenação de Aperfeiçoamento de Pessoal de Nivel Superior (CAPES, Brazil).

[1] Y. Aoki, G. Endrodi, Z. Fodor, S. D. Katz, and K. K. Szabo, Nature (London) **443**, 675 (2006).
[2] M. Asakawa and K. Yazaki, Nucl. Phys. A **504**, 668 (1989).
[3] A. Barducci, R. Casalbuoni, S. De Curtis, R. Gatto, and G. Pettini, Phys. Lett. B **231**, 463 (1989).
[4] A. Barducci, R. Casalbuoni, G. Pettini, and R. Gatto, Phys. Rev. D **49**, 426 (1994).
[5] M. A. Halasz, A. D. Jackson, R. E. Shrock, M. A. Stephanov, and J. J. M. Verbaarschot, Phys. Rev. D **58**, 096007 (1998).
[6] K. Fukushima, J. Phys. G **35**, 104020 (2008).
[7] J. Berges and K. Rajagopal, Nucl. Phys. B **538**, 215 (1999).
[8] O. Scavenius, A. Mòcsy, I. N. Mishustin, and D. H. Rischke, Phys. Rev. C **64**, 045202 (2001).
[9] M. A. Halasz, A. D. Jackson, R. E. Shrock, M. A. Stephanov, and J. M. Verbaarschot, Phys. Rev. D **58**, 096007 (1998).
[10] Y. Hatta and T. Ikeda, Phys. Rev. D **67**, 014028 (2003).
[11] K. Fukushima, Phys. Rev. D **78**, 114019 (2008).
[12] E. S. Bowman and J. I. Kapusta, Phys. Rev. C **79**, 015202 (2009).
[13] J. I. Kapusta and E. S. Bowman, Nucl. Phys. A **830**, 721C (2009); in *CPOD2009 Proceedings*, PoS(CPOD2009)018 (SISSA, Trieste, Italy, 2009).
[14] Z. Zhang and T. Kunihiro, arXiv:1005.1882 [hep-ph].
[15] C. Schmidt, PoS **LAT2006**, 021 (2006).
[16] P. de Forcrand and O. Philipsen, J. High Energy Phys. 11 (2008) 012; 01 (2007) 077; P. de Forcrand, S. Kim, and O. Philipsen, PoS **LAT2007**, 178 (2007).
[17] L. Ferroni and V. Koch, arXiv:1003.4428 [nucl-th].
[18] R. D. Pisarski and F. Wilczek, Phys. Rev. D **29**, 338 (1984).
[19] V. Skokov, B. Friman, E. Nakano, K. Redlich, and B. J. Schaefer, Phys. Rev. D **82**, 034029 (2010).

[20] A. F. S. Moreira, W. Figueiredo, and V. B. Henriques, Phys. Rev. B **66**, 224425 (2002).

[21] E. S. Fraga and A. J. Mizher, Phys. Rev. D **78**, 025016 (2008); Nucl. Phys. A **820**, 103c (2009).

[22] R. Seznec and J. Zinn-Justin, J. Math. Phys. **20**, 1398 (1979); J. C. Le Guillou and J. Zinn-Justin, Ann. Phys. (NY) **147**, 57 (1983); V. I. Yukalov, Moscow Univ. Phys. Bull. **31**, 10 (1976); W. E. Caswell, Ann. Phys. (NY) **123**, 153 (1979); I. G. Halliday and P. Suranyi, Phys. Lett. B **85**, 421 (1979); J. Killinbeck, J. Phys. A **14**, 1005 (1981); R. P. Feynman and H. Kleinert, Phys. Rev. A **34**, 5080 (1986); H. F. Jones and M. Moshe, Phys. Lett. B **234**, 492 (1990); A. Neveu, Nucl. Phys. B, Proc. Suppl. **18**, 242 (1990); V. Yukalov, J. Math. Phys. **32**, 1235 (1991); C. M. Bender, F. Cooper, K. A. Milton, M. Moshe, S. S. Pinsky, and L. M. Simmons, Phys. Rev. D **45**, 1248 (1992); H. Yamada, Z. Phys. C **59**, 67 (1993); A. N. Sissakian, I. L. Solovtsov, and O. P. Solovtsova, Phys. Lett. B **321**, 381 (1994); C. Arvanitis, F. Geniet, M. Iacomi, J.-L. Kneur, and A. Neveu, Int. J. Mod. Phys. A **12**, 3307 (1997); H. Kleinert, Phys. Rev. D **57**, 2264 (1998); Phys. Lett. B **434**, 74 (1998); for a review, see H. Kleinert and V. Schulte-Frohlinde, *Critical Properties of* ϕ^4*-Theories* (World Scientific, Singapore, 2001), Chap. 19; K. G. Klimenko, Z. Phys. C **50**, 477 (1991); H. Kleinert and V. Schulte-Frohlinde, *Critical Properties of Phi**4-Theories, River Edge, USA* (World Scientific, 2001), p. 489; K. G. Klimenko, Mod. Phys. Lett. A **9**, 1767 (1994); S. Chiku and T. Hatsuda, Phys. Rev. D **58**, 076001 (1998).

[23] J. Zinn-Justin, arXiv:1001.0675 [math-ph]; J. Zinn-Justin and U. D. Jentschura, J. Math. Phys. **51**, 072106 (2010).

[24] F. F. de Souza Cruz, M. B. Pinto, and R. O. Ramos, Phys. Rev. B **64**, 014515 (2001); J.-L. Kneur, A. Neveu, and M. B. Pinto, Phys. Rev. A **69**, 053624 (2004); B. Kastening, *ibid.* **70**, 043621 (2004); J.-L. Kneur and M. B. Pinto, *ibid.* **71**, 033613 (2005).

[25] J.-L. Kneur, M. B. Pinto, and R. O. Ramos, Phys. Rev. Lett. **89**, 210403 (2002); Phys. Rev. A **68**, 043615 (2003); E. Braaten and E. Radescu, Phys. Rev. Lett. **89**, 271602 (2002); Phys. Rev. A **66**, 063601 (2002).

[26] J.-L. Kneur, M. B. Pinto, R. O. Ramos, and E. Staudt, Phys. Rev. D **76**, 045020 (2007); Phys. Lett. B **657**, 136 (2007).

[27] J. B. Kogut and C. G. Strouthos, Phys. Rev. D **63**, 054502 (2001).

[28] J. O. Andersen, E. Braaten, and M. Strickland, Phys. Rev. Lett. **83**, 2139 (1999); Phys. Rev. D **61**, 014017 (1999); J. O. Andersen, M. Strickland, and N. Su, Phys. Rev. Lett. **104**, 122003 (2010).

[29] J.-L. Kneur and A. Neveu, Phys. Rev. D **81**, 125012 (2010).

[30] J.-L. Kneur, M. B. Pinto, and R. O. Ramos, Phys. Rev. C **81**, 065205 (2010).

[31] V. Koch, T. S. Biro, J. Kunz, and U. Mosel, Phys. Lett. B **185**, 1 (1987).

[32] A. Mocsy, I. N. Mishustin, and P. J. Ellis, Phys. Rev. C **70**, 015204 (2004).

[33] J. I. Kapusta and C. Gale, *Finite-temperature Field Theory: Principles and Applications* (Cambridge University, Cambridge, UK, 2006), p. 428.

[34] I. J. R. Aitchison and C. M. Fraser, Phys. Rev. D **31**, 2605 (1985).

[35] G. W. Carter, P. J. Ellis, and S. Rudaz, Nucl. Phys. A **618**, 317 (1997).

[36] G. W. Carter, O. Scavenius, I. N. Mishustin, and P. J. Ellis, Phys. Rev. C **61**, 045206 (2000).

[37] M. I. Gorenstein and S. N. Yang, Phys. Rev. D **52**, 5206 (1995).

[38] Y. Nambu and G. Jona-Lasinio, Phys. Rev. **122**, 345 (1961); **124**, 246 (1961).

[39] M. Buballa, Phys. Rep. **407**, 205 (2005).

[40] P. M. Stevenson, Phys. Rev. D **23**, 2916 (1981); Nucl. Phys. B **203**, 472 (1982).

[41] J.-L. Kneur, M. B. Pinto, and R. O. Ramos, Phys. Rev. D **74**, 125020 (2006).

[42] P. Costa, H. Hansen, M. C. Ruivo, and C. A. de Sousa, Phys. Rev. D **81**, 016007 (2010).

[43] H. Dosch and S. Narison, Phys. Lett. B **417**, 173 (1998).

[44] L. Giusti, F. Rapuano, M. Talevi, and A. Vladikas, Nucl. Phys. B **538**, 249 (1999).

[45] H. Mao, J. Jin, and M. Huang, J. Phys. G **37**, 035001 (2010).

[46] D. Kharzeev and K. Tuchin, J. High Energy Phys. 09 (2008) 093; F. Karsch, D. Kharzeev, and K. Tuchin, Phys. Lett. B **663**, 217 (2008).

[47] H. Fujii and M. Ohtani, Phys. Rev. D **70**, 014016 (2004).

[48] P. Costa, M. C. Ruivo, and C. A. de Souza, Phys. Rev. D **77**, 096001 (2008).

[49] Y. G. Ma *et al.*, Phys. Rev. C **71**, 054606 (2005).

[50] B. J. Schaefer and J. Wambach, Phys. Rev. D **75**, 085015 (2007).

[51] C. R. Allton *et al.*, Phys. Rev. D **71**, 054508 (2005).